Journal of Materials Chemistry C

Accepted Manuscript

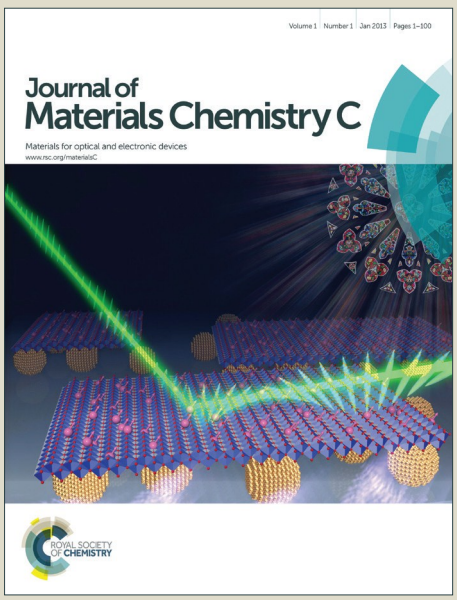

ROYAL SOCIETY OF CHEMISTRY

www.rsc.org/materialsC

Effect of Fe-doping on structure and magnetoelectric properties of $(Ba_{0.85}Ca_{0.15})(Ti_{0.9}Zr_{0.1})O_3$ synthesized by chemical route

E.Venkata Ramana[1*], F.Figueiras[2], A.Mahajan[3], David Maria Tobaldi[4], Benilde F.O. Costa[5], M.P.F.Graça[1] and M.A.Valente[1]

[1] I3N-Aveiro, Department of Physics, University of Aveiro, Aveiro-3810 193, Portugal.

[2] CICECO, University of Aveiro, Aveiro-3810 193, Portugal.

[3] School of Engineering and Material Science, Queen Mary University of London, London, E1 4NS, UK.

[4] Department of Materials and Ceramics Engineering / CICECO, University of Aveiro, Aveiro-3810 193, Portugal.

[5] CFisUC, Department of Physics, University of Coimbra, Coimbra-3004 516, Portugal.

* Author for correspondence: venkataramanaesk@rediffmail.com

B-site Fe-doped $(Ba_{0.85}Ca_{0.15})(Ti_{0.9}Zr_{0.1})O_3$ was synthesized by a facile chemical route to study the effect of doping on its physical properties. Detailed analysis of x-ray diffraction and Raman spectroscopy revealed an increased lattice strain and thereby deviation from morphotropic phase boundary with the progressive doping of Fe from 1 to 5 mol. %. Such structural changes have resulted in the weakening of energy band gap as well as deterioration of ferroelectric polar nature which was evidenced by a shift of tetragonal to cubic transitions towards room temperature and hard doping effects in ferroelectric hysteresis. The doped samples exhibited room temperature ferromagnetism. Combined Mossbauer and X-ray photoelectron spectroscopic studies suggest that oxygen vacancies and defect complexes induced by it play a major role in magnetic properties. Local piezoresponse measurements illustrated imprint characteristics of ferroelectric domains in undoped and doped samples at nanoscale. Room temperature magnetoelectric (ME) measurements revealed that 1 mol. % Fe doped sample, having higher ferroelectric polarization and moderate magnetization, exhibits a strong ME response with a coefficient of 12.8 mV/cm-Oe. The present study on Fe-doping effects on structure and related ME properties of this important lead-free material is useful to tailor multiferroic applications in electronics.

1. Introduction

Recently the study of materials, with coexistence of long-range ferroic orders and strong coupling between pertinent order parameters, has been a focus of attention for scientific community, in view of their potential technological applications. Such multiferroic magnetoelectric (ME) materials can possess variety of applications such as sensors, multistate memories and actuators in the field of electronics as well as in biomedical fields [1,2,3]. In single phase, $BiFeO_3$ is the only known material that exhibits room temperature ME coupling reported till now. Due to this, the approach of integrating ferromagnetic and ferroelectric oxides by means of bilayers in 2-2 connectivity was proven to be successful to achieve giant ME coupling [4]. However, engineering multiferroics and study the sublattice interactions of various ferroic orders in single phase materials are interesting to fabricate materials for future device applications.

Ferroelectric perovskite $BaTiO_3$ (BTO) and its solid solutions are an important class of materials that show large piezoelectric response and high dielectric constant useful for technological applications such as transducers, ferroelectric random access memories (FeRAM) and surface acoustic wave (SAW) devices [5]. BTO is a classical ferroelectric and intrinsic non-magnetic due to a formal d^0 electronic configuration of Ti^{4+} that drives cation off-centering for ferroelectric order. However, partially filled *d* state is required for magnetic order. On the other hand recent studies demonstrated dilute magnetic order in nanocrystalline BTO at room temperature, due to oxygen vacancy concentration [6, 7]. In addition doping transition metals (TM) such as Fe, Co, Cr, Mn also benefitted BTO to exhibit ferromagnetic properties. In these doped ones oxygen vacancies and hybridization between *p* and *d* orbitals of O and TM atoms, favor the exchange interactions among local moments that results in ferromagnetism [8]. In

literature several researchers reported on the multiferroic nature of doped BTO in thin films and bulk. Dang *et al*. [9] reported the threshold of phase separation between tetragonal-hexagonal structure at a concentration of 0.5 mol. % and ferromagnetic interactions above 6 mol. % Fe doping in $BaTiO_3$ ceramics. On the other hand Ray *et al*. [10] demonstrated hexagonal structure for 1 mol. % Fe-doped BTO single crystals and room temperature ferromagnetism for 5 mol. % doping. Wei *et al.* [11] presented room temperature weak ferroelectricity and ferromagnetism in highly Fe-doped BTO (> 33 mol. %). Huang *et al*. [12] observed a non-monotonic variation of aging behavior in Fe-doped $BaTiO_3$ ceramics (for Fe ≤ 2 mol. %) contributed by the competitive interaction of oxygen vacancies and structural variations. Ju *et al*. [13] found multiferroic behavior induced by Cr doping in BTO nanoparticles. In our previous work we observed room temperature multiferroic properties with complete 180^o domain reversal for Fe ≤ 20 mol. % doped BTO epitaxial thin films [14].

In a recent advancement in piezoelectrics, Liu and Ren [15] observed a large piezoelectric coefficient, $d_{33} \geq 600$ pC/N, in (1-x) $Ba(Ti_{0.8}Zr_{0.2}O_3) - x\ (Ba_{0.7}Ca_{0.3})TiO_3$ (BZT-BCT) solid solutions with a morphotropic phase boundary (MPB) at x=0.5 , a value larger than soft $Pb(Zr,Ti)O_3$ (PZT) . The phase diagram of this compound is similar to that of PZT in a way that it consists of paraelectric cubic (C) and two ferroelectric phases rhombohedral (R) and tetragonal (T). In a recent study, Xue *et al*. [16] reported electromechanical coupling factor, K_P = 65%, piezoelectric voltage coefficient $g_{33} = 15.3 \times 10^{-3}$ Vm/N and elastic constant S^E_{33}=19.7 p m^2/N, which are superior to PZT. The strong piezoelectric response observed for x=0.5 sample is interpreted in terms of isotropic flattering of a free energy profile associated with C-R-T triple point or tricritical point. Gao *et al*. [17] observed that strong piezoelectric character near MPB is due to easy polarization rotation between the coexisting nano-scale tetragonal and

rhombohedral domains. Thus this material with superior piezoelectricity attracted large applications as energy harvesters, sensors and actuators. Yuan *et al*. [18] found that BZT-BCT nanowires can be extremely useful in nanogenerators for powering implantable medical devices which are biocompatible.

In view of reported multiferroic properties in FM doped BTO and larger piezoelectricity in BZT-BCT, it is interesting to study phase stability and physical properties of the latter, with FM doping. For this purpose, we synthesized Fe-doped $(Ba_{0.85}Ca_{0.15})(Ti_{0.9}Zr_{0.1})O_3$ (BCTZO) nanoparticles by a chemical method. Structural, ferroelectric, magnetic and ME properties are studied. Ferroelectric imprint was observed by piezoresponse force microscopy.

2. Experimental

Nanoparticles of pristine, 1 mol. %, 2 mol. % and 5 mol. % Fe-doped BCTZO were synthesized following sol-gel method. In a typical synthesis barium acetate $[Ba(C_2H_3O_2)_2]$, calcium acetate $[Ca(C_2H_3O_2)_2]$, tetrabutyl titanate $[C_{16}H_{36}O_4Ti]$, zirconium acetylacetonate $[Zr(C_5H_7O_2)_4]$ and iron nitrate $[Fe(NO_3)_3]$ were used as precursor materials. Glacial acetic acid and 2-methoxyehtanol (2-MOE) were taken as solvents and chelating agents. First, 0.2 M barium acetate and calcium acetate were dissolved in acetic acid kept under vigorous stirring at 105 °C for 1 h. A 0.2 M titanate solution was prepared by dissolving tetrabutyl titanate in 2-MOE and stirred at 60 °C for 30 min. To this, stoichiometric amount of Zr-acetylacetone was added and stirred for 1 h. Now this Ti+Zr containing solution was added drop wise to the Ba+Ca solution at 60 °C to obtain a clear transparent solution. The final solution was refluxed at 100 °C for 4 h to obtain a pale yellow BCTZO solution which was subsequently heated at 120 °C to form a brown colored gel. The gel was then kept in an oven at 250 °C to obtain a

xerogel, which was heat treated at 800 ^{o}C in a furnace to obtain BCTZO nanoparticles. For Fe-doped samples the above procedure is followed after adding stoichiometric amount of iron nitrate to the Ti-solution. The above powders were uniaxially pressed into cylindrical discs of 8 mm diameter at 5 MPa and sintered at 1480 ^{o}C for 3 h.

X-ray powder diffraction (XRD) data for the structural characterization were collected using a Phillips X-ray diffractometer, equipped with a fast RTMS detector (PIXcel, 1D linear), with graphite monochromated Cu K_{α} radiation (45 kV and 40 mA, 2θ range of 10 - 120 °, a virtual step scan of 0.01 ° 2θ and virtual time per step of 798 s). For this purpose, sintered discs were crushed into powders and heat treated at 400 ^{o}C to relieve mechanical strains. Rietveld refinements on the full profile fitting of the XRD patterns were accomplished using the GSAS package [19], and its graphical user interface EXPGUI [20] . The particle size, structural analysis and chemical composition by energy dispersive spectroscopy (EDS) were analyzed by transmission electron microscopy (TEM, JEOL2200FS, 200 kV and FEI Titan, 300 kV). For TEM and EDS analyses, the nanoparticles of doped BCTZO were dispersed in chloroform by ultra-sonication for 5 min, and then the solutions were dropped on a copper grid coated with holey carbon film. Raman spectra were measured on nanoparticles using the micro-Raman spectrometer (Horiba Jobin Yvon) with a 633 nm excitation laser, an edge filter for Rayleigh line rejection, and a CCD detector. The laser was focused on the sample to a spot size of ~2 μm using a 50 x objective lens. Surface morphology of the sintered ceramics was observed by the scanning electron microscope (SEM, Hitachi S-4100). For electrical measurements gold electrodes were sputtered on polished ceramic specimens. Dielectric measurements were carried out in the frequency range 0.1–500 kHz in the temperature range 200 – 400 K using an impedance analyzer (Agilent 4294A). Polarization-electric field hysteresis loops were measured using the hysteresis loop tracer TF-Analyzer (aixACCT). Electrical poling

was performed in the field range 40-60 kV/cm for 30 min at 50 ^{o}C in silicone oil (Merck) bath and field cooled to room temperature. Piezoelectric charge coefficient (d_{33}) was measured on poled samples using a piezometer (PM100), after aging them for 24 h. Local piezoresponse was visualized using a commercial scanning probe microscope (Ntegra Prima, NT-MDT) equipped with an external lock-in amplifier (SR 830, Stanford Research) and a function generator (Yokogawa, FG 120). Here, we used commercial Phosporous doped Si probes (NANOSENSORS) with a radius of curvature R<10 nm and resonance frequency 13 kHz and spring constant (k) = 0.2 N/m. Temperature dependent magnetization was measured using a vibrating sample magnetometer (Cryogenic). Zero field cooled (ZFC) and field cooled (FC) magnetization was measured under H=1 kOe**.** X-ray photoelectron spectra (XPS) measurements were performed using a Kratos Axis Ultra HAS Spectrometer (Kratos Analytical, Manchester, UK) with a monochromatic Al K X-ray source (1486.6 eV) operating at 150 W under 1.0×10^{-9} Torr.

The ^{57}Fe Mössbauer spectra were recorded at room temperature in transmission geometry in a constant acceleration type spectrometer using a 57Co/Rh source with strength of about 10 mCi. The fitting of the spectra was carried out with a set of Lorentzian lines, determined by least squares minimization, using the fitting program NORMOS, distributed by Wissel (Germany). The isomer shifts are referenced to α-Fe at room temperature. Magnetoelectric measurements were carried out using the dynamic ME method using an in-house experimental set-up [21]. The voltage output generated from the sample under magnetic field was measured by the lock-in amplifier (Stanford, SR530).

3. Results and discussion

Fig. 1 shows the powder XRD patterns of pure and Fe-doped BCTZO. All the samples exhibited typical perovskite diffraction peaks, which can be indexed based on standard XRD data of tetragonal $BaTiO_3$ with *P4mm* space group. The absence of additional peaks apart from the perovskite phase indicates the formation of high purity BCTZO for doping concentrations up to 5 mol. % of Fe. For pure and doped samples the characteristic peak around $2\theta=31.6^{o}$ is split into (101)/(110) reflections similar to the earlier observation of BCTZO, representing the tetragonal phase. Similarly, the observation of (002)/(200) tetragonal peak splitting around $2\theta=45^{o}$ for all the samples confirms the rhombohedral/tetragonal coexistence (softening for Fe-5), a feature that is characteristic for composition at MPB in BCTZO [15, 22]. Similar trend was observed for (202)/(220) peak splitting around $2\theta = 65.9^{o}$. Such a splitting is expected due to the electrostatic repulsion between 3*d* electrons of Ti^{4+} and 2p electrons of O^{2-} ions resulting in a distorted perovskite with tetragonal character. Softening of peak splittings for higher Fe-doping indicates the decrease in tertagonality. At the same we observe a peak split of (222) reflection around $2\theta = 84^{o}$ (dominant in Fe-1and Fe-2 samples), a feature of R phase which also softens for Fe-5 doping. A peak fitting of (101)/(110) and (002)/(200) reflections is shown in the inset of fig. 1. The systematic shift of characteristic peak around $2\theta = 31.6$ (inset of fig. 1) towards lower 2θ position indicates

a strain in BCTZO lattice resulting in the expansion of unit cell volume. The merging or reduction in the splitting of (101)/(110) and (002)/(200) with composition indicates either tetragonal to rhombohedral transformation or reduction of tetragonality.

To quantify the existence of R and T phases and the effect of Fe on phase stability, we performed refinements using the GSAS software. The resulting graphic output is shown in Fig.2, while Rietveld agreement factors as well as the phase composition of the specimens are reported in Table 1. For undoped BCTZO, the ratio between the tetragonal and rhombohedral phases is around 61:39. This gradually increases with the iron doping, roughly being 91:9 in Fe-1, and 92:8 in Fe-2. The doping of 5 mol. % of Fe led to a complete transformation of MPB phase into a stable tetragonal phase. The lattice parameters were calculated from Rietveld refinement and results are enlisted in Table 2. The observed tetragonal lattice parameters (a = 3.9715 Å and c = 4.0007 Å) for Fe-0 sample are smaller compared to our previous work[19] and report by Liu and Ren (a = 4.007 Å and c = 4.025 Å) [15] which may be due to different synthesis conditions (synthesized by the ceramic rout and sintered at 1500 ^{o}C). With the increase in Fe content an increase in 'a' and decrease in 'c' can be seen. Such a lattice distortion is expected due to the replacement of larger Fe^{3+} (0.645 Å) into Ti^{4+} (0.605 Å) atoms, leading to the creation of oxygen vacancies in order to maintain charge neutrality, following the relation $Fe_2O_3 + 2Ti_{Ti} + O_O \rightarrow 2Fe'_{Ti} + V_O^{\cdot\cdot} + 2TiO_2$ ……(1)

It is also possible that Fe^{3+} may partially substitute Zr^{4+} (0.72 Å). In case Fe substitutes Zr sites, one can expect a reduction in lattice parameters and increased tetragonal strain, similar to Fe-doped PZT (at Zr-Site) [23], which is the converse to the present observation. Meanwhile, the systematic decrease in c/a ratio indicates the suppression of ferroelectric distortion. The change in c/a for Fe-0 to Fe-5 sample is ~ 1.1 % as Fe^{3+} is nearly 6.6 % larger than Ti^{4+}. Such a change in strain corresponds to a

chemically induced pressure > 6 GPa as calculated from change in unit cell volume with a hydrostatic pressure in BTO single crystals [24]. From these results we conclude that doping Fe induces a compressive strain in unit cell resulting in the transformation of BCTZO from MPB state to pseudo cubic lattice.

Complete details on crystal structure are presented in Table 2 (unit cell parameters and unit cell volumes, tetragonality, atomic positions and U_{iso}), and Table 3 (*A*−O and *B*−O bond length distances). As it is seen in Table 2, the unit cell volume of the tetragonal phase is subjected to an expansion, while the rhombohedral angle is close to 90 ^{o}. Looking at the bond length distances, Table 3, it is observed that the BO_6 octahedral site in BCTZO is the most distorted one amongst the series, having *D* value equal to 0.0539, and a QE value of 1.0222 (*cf* Table 3). In it, the difference between the two apical *B*−O1 distances is also the greater amongst the series – in this case we can invoke a pseudo Jahn-Teller effect [25]. On the other hand, iron doping gradually decreases the difference between the two apical *B*−O1 distances, as well as the octahedral distortion of BO_6 site. Here, the Fe-5 sample has lower *D* value, and QE value roughly the same as Fe-2 (*cf* Table 3). This is visualized by the 3D rendering of the tetragonal phase in Fe-0 and Fe-5; the corresponding BO_6 octahedra are illustrated in the inset of fig. 2 (a) and (b). However, in this regard, it has to be underlined that QE gives a quantitative measure of polyhedral distortion, which is independent of the effective size of the polyhedron; by contrast, the Baur distortion index *D* takes into account merely the metal–ligand distances and the average bond length distance [26].

The size and composition of these nanoparticles was analyzed by TEM. Fig. 3 (a) shows the representative high resolution (HR) TEM image of Fe-2 sample nanoparticles heat treated at 800 ^{o}C. The average particle size was observed to be in the range 24 - 33 nm which is good agreement with that calculated from XRD using

Scherrer equation. The TEM image shows lattice fringes with inter planar distance of ~0.282 nm corresponding to {110} reflection of BTO tetragonal lattice (inset of fig. 1 a) and indicates that the nanoparticles have continuous crystalline lattices. To ascertain the composition we measured EDS mapping from the area shown fig.3 (a) and the corresponding elemental distribution pattern is shown in fig. 3 (b). The EDS image depicts the detection of Ba, Ca, Ti, Zr and Fe metal elements in Fe-2 sample. The measured atomic percentage of elements are in good approximation of expected ratios; theoretical (and measured) atomic percentage of Ba: Ca: Ti: Fe: Zr are 42.5(41.7):7.5(7.2):44(44.7):1(0.94):5(4.8).

To find the effect of Fe-doping on structure, Raman spectroscopic measurements were carried out. The tetragonal BTO (*P*4*mm*) in general exhibits three [A_1(TO)+A_1(LO)], one B_1 and four [E(TO+LO)] Raman active modes around wavenumbers 250, 307, 515, 715 cm^{-1} respectively along with several weak modes [27]. Fig. 4 (a) shows the compositional dependent Raman spectra at room temperature. Pristine BCTZO and doped samples exhibit major peaks around 210, 295, 523, 726 cm^{-1} represented by A_1(TO), B_1/E(TO+LO), (A_1, E(TO)), (A_1(LO), E(LO)) character and weaker modes around 141, 171, 240 cm^{-1} with A_1(TO), E(TO)/E(LO)/A_1(LO), A_1(TO) respectively. The observed Raman modes are consistent with earlier reports on BCTZO [22, 28]. The Raman active asymmetric breathing mode (A_{1g}) around 830 cm^{-1} grows with the increase of Fe doping in BCTZO (shown in fig. 4 b), which is absent for BTO. It is reported in literature [29] that the relative intensity of the A_{1g} mode is qualitatively related to the concentration of species replacing Ti in the B-site. This observation quantifies the progressive doping of Fe at B-site. For solid solutions having two or more B-site species, A_{1g} mode becomes Raman active due to the presence of dissimilar ions at the

centre of the octahedra that creates asymmetry in breathing-like mode, which is reported to be strictly chemical nature but not connected to structural distortions. With the increase in Fe content, the observation of systematic shift in several Raman modes towards lower wavenumber indicates the compressive stress induced by doping ions. The anti-symmetry mode A_1 (TO) around 210 cm^{-1} has become broad and shifted towards the lower frequency region (190 cm^{-1} for Fe-5 sample), which is ascribed to the asymmetric Ti–O phonon vibrations. The observation of A_1 (TO) mode around 520 cm^{-1} is due to O–Ti–O symmetric stretching vibrations. These modes correspond to higher concentrations of polar octahedral, tetragonally distorted clusters in BTO matrix. As the atomic mass of Fe is larger than Ti, Raman shift of former is larger than the later in accordance with $w=(1/2\pi)\times(k/m)^{1/2}$. The observation of mode with B_1/E (TO+LO) character around 295 cm^{-1} indicates the asymmetry of TiO_6 octahedra and is signature of tetragonal phase. Thus, a careful examination of this peak shows that the structure of Fe-doped BCTZO is tetragonal, even for 5 mol. % Fe doped BCTZO sample. It was reported that Fe-doped BTO exhibits an intense peak in Raman spectra around 640 cm^{-1} that characterizes hexagonal phase [9], which is absent in the present work indicating no phase transformation. At the same time, suppression of vibrational intensities of all the Raman modes (especially around 295 cm^{-1}) with Fe doping clearly suggests the decrease of tetragonality and stretching of Ti-O bond distances. It can be assumed that the distribution of FeO_6 clusters into the lattice may reduce the dipolar interaction between TiO_6 polar clusters. Thus the combination of Raman and XRD results indicates the presence of non-centrosymmetric regions due to the off-centering of Ti/Zr/Fe atoms and reduction in tetragonality, thereby polar ferroelectric nature, for higher Fe-doping.

Fig. 5 shows the UV-Vis diffused reflectance spectra measured on different BCTZO nanoparticles. The absorption edge of pristine BCTZO was observed at 373

nm, which is similar to BTO. With the increase in Fe content absorption edge becomes smoother and wider. A shift in this peak edge towards higher wavelength is due to the replacement of Fe at the Ti-site. Optical absorption in the BTO-based oxides arises due to the transition from O 2p valence band (VB) to Ti 3d conduction bands. The observed red shift of the absorption edge demonstrates that electronic jump to the conduction band is easier in the Fe-doped BCTZO compared to Fe-0 samples, resulting in a decrease of resistivity. The optical band gap (E_g) energy calculated from the fig. 5 (inset) is ~ 3 eV for BCTZO, which is slightly smaller compared to that of BTO (3.2 eV) in bulk. The samples doped with 1, 2 and 5 mol. % Fe show an E_g of 2.6, 2.3 and 1.8 eV respectively. Such shrinkage in energy levels was also reported by Dang *et al* [9] in Fe-doped BTO ceramics. In a recent theoretical study, Bennet *et al*. [30] predicted that the oxygen vacancy in doped BTO introduces additional energy states in the vicinity of top of the valence band and bottom of the conduction band. In the present study, the increase in concentration of Fe ions at Ti^{4+} and creation of $V_O^{\cdot\cdot}$ can cause the overlapping of absorption regions, resulting in narrow band gap. As a consequence of the formation of new states in the energy band structure, a decrease of band gap is expected. In other words, the smaller E_g values are related to the presence of intermediary energy levels which were generated from 3*d* electrons of Fe ions or defects. Here it is noteworthy that the energy levels in a crystal lattice are dependent on the degree of structural disorder. Therefore, the increase of structural disorder in the present system (Table 1) leads to an increase of intermediate energy levels and consequently decreased E_g.

The surface microstructure of sintered BCTZO samples observed by SEM is shown in fig. 6. The presence of well-developed and single shaped grains confirms the pure phase without any secondary phase. A dense granular structure with well-defined

grain boundaries can be observed for all the studied samples with non-uniform grain size distribution. It is seen that the grain size is strongly influenced by the amount of Fe content. The Fe-0 sample has an average grain size of 11.2 μm. As the content of Fe increases, the grain size decreases to 8.4, 4.1 and 1.8 μm for Fe-1, Fe-2 and Fe-5 samples respectively. This reduction in grain size suggests that the incorporation of Fe^{3+} ions can restrain grain growth in the BCTZO ceramics and the grain size decreases sharply when Fe content is ≥ 2 mol. %. The growth mechanism occurs by the grain boundary motion due to a reduction of the total grain boundary surface energy. The thermal energy leads to an increase in the diffusion rate and consequently intensifies the formation of necks between grains [26]. The reason for the decrease of grain size can be explained based on the ionic radii of Ti^{4+} and Fe^{3+} ions. Since ionic radius and atomic weight of Fe are larger than that of Ti, higher Fe doping results in less mobility of the ions causing an inhibited grain growth. In addition segregation of Fe atoms at grain boundaries for higher doping concentrations would also result in the reduced grain growth. Here, it is relevant to correlate grain size variations to the structural changes. The lattice distortion along the tetragonal *c*-axis is strongly reduced as the grain size shrinks to 1.8 μm (Fe-5), whereas the *a*-axis shows an enlargement of above 1 %. At the same time the crystal tetragonality decreases by 1.05% as the grain size decreases. These dimensional changes are expected to be results of an increase in the internal stress in the ceramic when the transition from a strongly ferroelectric MPB phase to near cubic ferroelectric phase occurs (Table 2). Similar observations were reported in several polycrystalline ferroelectrics [31, 32]. The spontaneous unit cell distortion is mutually clamped in the fine-grained materials that can cause a reduction in the intrinsic polarization and also increases the internal stress in the ceramic. This result is consistent with the observation of distortion in tetragonality observed from Raman measurements.

To study compositional dependence on ferroelectric phase transitions, we measured dielectric properties as a function of temperature in the frequency range 100 Hz – 1 MHz. Fig. 7 (a) shows the variation of dielectric permittivity (ε_r') of Fe-doped BCTZO samples at 1 kHz. The nature of ferroelectric transition for Fe-0 and Fe-5 samples at selected frequencies is shown in the inset. BCTZO sample exhibited an increase in ε_r' with temperature showing two distinct peaks: a broad hump at 43 ^{o}C and dielectric maxima at 92 ^{o}C. The observation of hump like behaviour confirms the coexistence of two phases, rhombohedral as well as tetragonal at room temperature and its polymorphic phase transition from R to T. The dielectric maximum corresponds to the Curie temperature (T_C) resulting from the tetragonal-cubic phase transition. The slight discrepancy in R-T transition temperature compared to previous work (around 30 ^{o}C) [15, 22] may be due to the synthesis conditions used in present study. For Fe-1 and Fe-2 samples both the phase transition temperatures (R-T, T- C) reduces to 11, 87.5 ^{o}C and 13, 81 ^{o}C respectively. In the case of Fe-5 sample a single broad peak was seen around 34 ^{o}C that corresponds to T - C transition while the R - T phase transition was completely diminished. The ferroelectric phase transition in present set of materials is due to the deformation of TiO_6 octahedra and the shift of T_C can be due to the distortion of Ti-O chains (B-O distance, Table 3) prompted by the creation of $V_O^{\cdot\cdot}$ due to Fe doping. The dielectric measurements are in good agreement with structural variations seen in XRD and Raman spectra that support the reduction of tetragonal strain due to Fe-doping.

These studies indicate that room temperature ferroelectric order exists up to Fe doping of 5 mol. %. On the other hand, nature of phase transitions becomes diffused and the order of diffusivity increases with the increase of Fe doping concentration,

albeit being non-relaxor. Such a phase transition is expected due to the presence of two or more heterovalent ions sharing A- and B-sites of lattice. The broadening of dielectric maxima in all the samples can also be correlated to the high degree of disorder at B-site that gives rise to the distribution of local Curie temperature.

The diffused phase transition is governed by a modified Curie-Weiss's law $\varepsilon = \frac{\varepsilon_{\max}}{1+(T-T_m)^{\delta}}$ described in literature [22,] here T_m refers to the temperature that corresponds to ε_{max}. The parameter δ = 1 corresponds to a classical ferroelectric transition while $\delta = 2$ describes the relaxor ferroelectric nature. The slope (δ) calculated from the log $(1/\varepsilon_r' - 1/\varepsilon_{r\,\max}')$ *vs*. log (T-T_m) plot (fig. 7 b) at 1 kHz (&100 kHz) for Fe-0, 1, 2 and 5 samples is 1.6 (1.5), 1.69 (1.62), 1.89 (1.7) and 1.97 (1.9) respectively, indicating the diffused phase transition introduced by the Fe-doping into ferroelectric lattice. The room temperature ε_r' for Fe-0 sample is 3400 which is in the same order reported in literature. With the increase in Fe-doping the value of ε_r' was found to decrease. The drop in this value with doping is due to the decrease in polarization. The change in ε_r' can also be considered as a result of combined intrinsic grain size effects causing a reduction of tetragonality and spontaneous polarization as well as extrinsic factors like low permittivity grain boundaries. As the grain size becomes lower, there exists lower permittivity non-ferroelectric grain boundaries which contribute to the drop in ε_r', demonstrated as the 'dilution effect' in literature [33, 34]. The existence of such low permittivity regions can be accounted for a perovskite shell with disordered/defective structure or with non-switchable polarization close to the surface of the grains [34]. In addition to above changes in ε_r', the shift of T_C towards lower temperatures can also be

accounted for the changes in grain size. The effect of grain size on the ferroelectric properties can be qualitatively described on the basis of the corresponding variation of the tetragonal strain in the framework of the Landau-Ginsburg-Devonshire theory [34]. The decrease in grain size, variation of the tetragonal strain and consequent modification of the spontaneous polarization affects the phase transitions and the ferroelectric properties. The room temperature dielectric loss for Fe-0 sample is 2.7% which increases to 5 % at T_C. With the increase in Fe-content, room temperature tan δ increases to 4.5 % (Fe-1), 7 % (Fe-2) and 12.3 % (Fe-5).

The piezoelectric coefficient was measured on poled samples at room temperature. BCTZO exhibited a d_{33} of 497 pC/N and a continuous drop was seen with the progressive replacement of Ti with Fe (274 pC/N, 172 pC/N and 101 pC/N for Fe-1, Fe-2 and Fe-5 samples respectively). As the d_{33} is related to polarization according to the relation $d_{33} = 2Q_{11}\varepsilon_o\varepsilon_r P$, ($Q_{11}$ is the electrostriction coefficient, $\varepsilon = \varepsilon_o\varepsilon_r$ is dielectric permittivity, P is the polarization), the decrease in its value is due to the decrease in spontaneous polarization. Fig. 8 (a) shows the polarization-electric field hysteresis loops for Fe-0, Fe-1, Fe-2 and Fe-5 samples. All the samples exhibited saturation within the applied field without dielectric breakdown. The remanent and saturation polarizations (P_r and P_S) of pristine BCTZO sample are 12.3 and 20.1 μC/cm^2 with coercive field (E_C) =1.9 kV/cm indicating soft ferroelectric nature, which is natural to BCTZO ceramics. With the increase in Fe content BCTZO exhibited a decreasing trend of polarization, possessing P_r (and P_S) of 6.6 (17.1), 5.3 (12.6) and 2.1 (8.4) μC/cm^2 respectively for Fe-1, Fe-2 and Fe-5 samples. At the same time systematic increase in E_C with Fe content (2.1, 2.8 and 3.5 kV/cm for Fe-1, Fe-2 and Fe-5 respectively) indicates the hard doped affect, which is common to acceptor doped ferroelectrics. The

increasing trend of E_C with doping may be due to the pinning of domain walls by defect centers such as $Fe_{Ti}^{'} - V_O^{\cdot\cdot}$. Here it is noteworthy that the E_C is also influenced by the domain size as well as the domain configurations which are affected by the reduction in grain size. All these features indicate unambiguous ferroelectric nature of doped specimens under study. Inset of fig. 8 (a) depicts the representative relation between P_r and applied electric field at 50 Hz for pristine and doped (Fe-1) samples. The observation of continuous drop in field derivative of P_r above 14 kV/cm for Fe-1 sample (compared to Fe-0), indicates that the saturation is slowly approached in doped samples. This suggests that the decreased polarization observed in doped samples (46 and 82 % drop in P_r for Fe-1 and Fe-5) can be associated with the decrease in spontaneous polarization as a function of grain size (11.2 μm for Fe-0 and 1.8 μm for Fe-5).

The observed changes in ferroelectricity can be linked to structural distortions observed by the rietveld analysis. The change in average B-O bond distance (shown in Table 3, 2.005 Å for Fe-0 and 2.008 Å for Fe-5 respectively) seems to influence the polarization which is the manifestation of BO_6 vibrations. A larger polarization is expected when an electric field is applied to a perovskite having larger B-site rattling space as they shift easily without disturbing the oxygen frame work [35]. With the addition of larger Fe ions, the rattling space available for smaller Ti/Zr ions is expected to reduce, resulting in a drop in polarization. In addition, reduced difference in *a* and *c* parameters routes to a diminished structural disorder that leads to the eventual drop in tetragonal to cubic phase transitions.

The hard ferroelectric properties observed in the present ceramics, relative to grain size, are well documented in literature [32, 36]. With the decrease in grain size, number of

90^o domain walls increases in accordance with the relation: the density of 90^o domain walls is in inversely proportional to the square root of grain size [36]. This indicates that with the decrease in grain size the distance dependent repulsive force between neighboring domain walls is enhanced. This leads to the reduction of domain wall mobility plus difficulty in domain reorientation against the applied electric field, resulting in the suppression of macroscopic polarization and increased E_C. The ferroelectricity in BTO based materials can be attributed to the formation of tetragonal structure. The polar nature with R-T-C triple point of current BCTZO suggests that an MPB composition is formed with larger grain size. The change in tetragonal strain, developed in view of the formation of small-sized grains in doped samples, is supposed to control the ferroelectricity.

Fig. 8 (b) depicts the electric field response of polarization current for Fe-0 and Fe-5 samples. The data shows important changes: i) observation of two peaks that indicate forward and backward domain switching of the ferroelectric state in these samples and ii) magnitude of I_P at the maxima is more than two folds larger for Fe-5 sample compared to the undoped one. The increased I_P (leakage) and decrease in polarization with doping may be due to the presence of oxygen vacancies formed as per the equation 1).

To ascertain the formation of $V_O^{\cdot\cdot}$ and related defects we performed X-ray photoelectron spectra of undoped and 5 mol. % Fe doped BCTZO samples. Fig. 9 shows the XPS data of Ti 2p core level peaks for Fe-0 and Fe-5 samples, while the O 1s core level spectra is shown in the inset. Ti 2p3/2 and 2p1/2 core level peaks were observed at 457.9 and 463.6 eV for Fe-0 sample while for Fe-5 they can be seen at 458 and 463.5 eV. The binding energy difference between $2p_{3/2}$ and $2p_{1/2}$ for both the samples is within 5.7 eV [37, 38]. This indicates that majority of Ti ions are in 4+ valence

state while we see no peak at lower binding energy that corresponds to Ti^{3+}. The shift in Ti 2p peaks may be due to the lattice distortion in 5 mol. % Fe-doped BCTZO. Furthermore, O 1s spectra show two peaks at 529.2 eV and 531.8 eV. The first peak corresponds to the lattice oxygen (Ti/Zr – O) while the smaller peak arises due to the oxygen vacancies [39]. Similar spectra can also be seen for Fe-0. The high and low intense peaks are labeled as O[1] and O[2] respectively. The observation of second peak at higher binding energy indicates the existence of $V_O^{\cdot\cdot}$ for undoped BCTZO which is expected for ferroelectric ceramics sintered at ambient temperatures. The increased intensity of O[2] peak for Fe-5 sample appears to be due to larger concentrations of $V_O^{\cdot\cdot}$ formed due to acceptor doping at B-site, resulting in the formation of charge defects mentioned in the earlier section.

To confirm piezo response (PR) at granular scale and to observe domain switching, we performed PFM measurements on pristine and Fe-doped BCTZO samples. Representative PFM images observed for Fe-2 sample are shown in fig. 10. Topography (fig. 10 a) is dominated by parallel grooves resulting from polishing process, while sporadic deeps are related to material detachment due to grain boundaries located near the surface. The out-of-plane PR amplitude and phase scans, presented in fig. 10 (b) and 10 (c) respectively, clearly show domains near 2 μm size, attesting genuine PR contrast without any visible cross-talk to topological grooves or defects, although it is possible that domain size and walls could be delimited by grains boundaries. Fig. 10 (d) and 10 (e) represent the PR amplitude and phase scans respectively, after bias lithography local poling experiments with ±20 V_{dc} (as outlined in fig.10 a). PR amplitude contrast patent in fig. 10 (d) reveals a clear imprint and domain reversal features with no visible surface damage, although PR phase visible in fig. 10 (e) do not present such strong response. In

order to distinguish between genuine piezo-response and electrostatic deflection between the tip and the sample surface, we performed experiments suggested by Balke *et al.* [40]. The relation between amplitude and phase PR is not necessarily proportional and depends on the local piezo and dielectric properties. Poor phase contrast can be explained by a relatively low dielectric loss between sample surface and tip [40]. Further evidence of local ferroelectric property is exemplified in fig. 10 (f) by piezoresponse hysteresis loops measured up to 40 V_{dc}, confirming the switchable ferroelectric state at nanoscale. Overall, PFM results evidenced the inherent ferroelectric character of Fe doped BCTZO samples, whose bulk polarization indicated a gradual loss with doping.

Room temperature magnetization measured for Fe-0, Fe-1, Fe-2 and Fe-5 samples is presented in fig. 11 (a). Undoped BCTZO shows an anti S-type hysteresis loop that constitutes diamagnetic nature. For samples with 1, 2 and 5 mol. % of Fe this diamagnetic signal gradually decreases and a feeble ferromagnetic loop was seen confirming long-range magnetic order. The room temperature saturation magnetization of Fe-1, Fe-2 and Fe-5 samples is 0.011, 0.025 and 0.056 emu/g. Fe-2 and Fe-5 samples show ferromagnetic nature at low fields and a linear increase in magnetization for field $\geq$ 5 kOe, with increase in linearization. This indicates that at higher Fe concentrations the present samples show competitive interactions between ferromagnetic and paramagnetic spins. Such a behavior may be expected due to the paramagnetic (PM) nature of Fe^{3+} ions. From M-T relation, an overlap of M_{ZFC} and M_{FC} curves was observed for all the doped samples, in the temperature range 5-300 K (not shown). The temperature dependent ZFC magnetization of Fe-1 sample is shown in Fig. 11 (b). It can be seen that the magnetization is higher at low temperatures and shows an exponential decrease with the increase in temperature. It was observed that for T < 20

K, antiferromagnetic/paramagnetic nature dominates while the ferromagnetic nature persists up to room temperatures. The hysteresis loops measured at different temperatures confirm this behavior (insert of fig. 11 b); M-H curve at 5 K shows paramagnetic or antiferromagnetic (AFM) nature and with the increase in T above 20 K, a transformation of linear M-H curve into S-type hysteresis loop was visible.

From our XPS analysis it was observed that with the increase in Fe content large numbers of oxygen vacancies are generated to maintain the charge neutrality (increase in intensity of peak at 531.8 eV). At the same time our XRD and TEM did not predict any impurities related to the presence of Fe_2O_3/Fe_3O_4. Thus the origin of FM nature of Fe-doped BCTZO is not external. Induced magnetization in the present samples can be explained based on the F-center mechanism proposed by Coey *et al*. in Fe-doped SnO_2 [41], Ren *et al.* in Fe-doped $PbTiO_3$ [42], TM doped $BaTiO_3$ (TM = Mn, Fe, Cr) [9, 14, 43]. According to this model, FM nature arises when the Fe^{3+} involves in a super exchange with Fe^{3+} through oxygen vacancy. An electron trapped in the oxygen vacancy constitutes an *F* center, where the electron occupies an orbital which overlaps the *d* shells of both iron neighbors. The exchange interaction between iron ions via F center is of FM nature, similar to the bound magnetic polaron. A similar scenario is expected in the present sample. Here, Fe^{3+} with $3d^5$ possesses unoccupied minority spin orbitals, the trapped electrons will be spin down and neighboring Fe^{3+} will be spin up to form $Fe^{3+} - V_O^{\cdot\cdot} - Fe^{3+}$ chains. Thus, the F center Fe^{3+} bonding leads to FM interaction while the superexchange interaction between paramagnetic Fe^{3+} ($Fe^{3+} - O^{2-} - Fe^{3+}$ chains) constitutes AFM/PM nature [41]. A competition between these components will lead to the observed changes mentioned in fig. 11.

To study the valence fluctuations in Fe, we performed XPS measurements on Fe-5 sample. The spectra indicated the existence of two wide bands at 712 and 724 eV. Due to the doping concentration and limitation of our instrument, the observed spectrum was quite noisy and difficult to fit for a meaningful discussion. For this purpose, we measured room temperature Mössbauer (MB) spectra. Fig 12 shows the room temperature Mössbauer spectra for Fe-2 and Fe-5 samples. The fitting parameters are shown in Table 4. At least two sub-spectra are required to fit Fe^{3+} ion sites. For lower Fe concentration (Fe-2 sample) one Fe^{3+} singlet needed to be included. No signature of Fe^{2+} has been found for which peaks at higher velocities should be seen. Also, Fe^{4+} ions are ruled out, as negative isomer shifts were needed to appear. From the present data it can be concluded that Fe-2 and Fe-5 samples are not of FM nature, in the absence of a sextet Mössbauer spectra. The low symmetry of spectra, as seen in fig. 12 are due to the presence of more oxygen vacancies- Fe dipoles interaction. The discrepancy observed in magnetic and MB spectra is similar to those observed in several diluted magnetic semiconductor (DMS) materials such as $Zn_{0.95}M_{0.05}O$ (M=Fe, Co) [44] and Fe-doped $BaTiO_3$ [45]. According to recent theoretical studies [46, 47], in perovskite ferroelectrics such as $BaTiO_3$ and $PbTiO_3$ oxygen and Ti defects could strongly influence ferromagnetism, while A-site defects do not. We haven't found any evidence on the presence of Ti^{3+} from this study while the presence of $V_O^{\cdot\cdot}$ is expected. According to results of fig. 5, these vacancies have influenced in the shift of Fermi energy level to form new states between valence and conduction bands. The density of states below Fermi level asymmetrically differs between the majority and minority spins. The spin-polarized states created in this manner could contribute to FM behavior.

To study the coupling between ferroic order parameters we measured ME measurements using the dynamic method. Samples were poled electrically under 35

kV/cm as well as magnetically at H=1 T using an electromagnet. ME measurements were performed by superimposing ac magnetic field (generated by Helmholtz coils) of 1 Oe at 1 kHz over a varying bias magnetic field (6 kOe). Here the reference signal was taken from signal generator feeding the Helmholtz coils. ME coefficient (α) was calculated by dividing voltage output by sample thickness and ac magnetic field. Fig. 13 shows room temperature magnetic field induced ME coefficient for Fe-1, Fe-2 and Fe-5 samples. ME output increases with the increase in H up to 1.4 kOe, attains a maximum and shows a decreasing trend with further increase in the field till 6 kOe. The trend of α *vs. H* is similar in all the samples while its magnitude is a function of doping concentration. Fe-1, Fe-2 and Fe-5 samples exhibited ME coefficient of 12.8, 7.0 and 2.9 mV/cm-Oe respectively. The present ME coefficient for Fe-1 is larger than experimental value of ~ 3.1 mV/cm-Oe reported for 1 mol. % Fe-doped BTO by Verma *et al.* [48], comparable to 13 mV/cm-Oe observed for 1.5 mol. % Cr-doped BTO by shah et al. [43] and smaller than 145 mV/cm-Oe reported by Kumari *et al.* [49] for 1.5 mol. % Fe-doped $Ba(Zr_{0.05}Ti_{0.95})O_3$.

The ME coupling in present materials is expected to occur due to local sub-lattice interactions between spin moments and disordered electric dipole moment. ME interactions are thus results due to magnetostriction (proportional to dM^2/dH^2) [4] of magnetic sub-lattice. By comparing M-H and α-H, it can be understood that the observation of increase in α for H ≤ 1.6 kOe is due to the growth of domains with favorable orientation to the field, and further growth of domains above this field decreases the deformation leading to the drop in α. The observation of ME coefficient even for 5 mol. % Fe-doped sample is due to the presence of tetragonal phase, unlike hexagonal features reported for 5 mol. % Fe doped BTO. The decrease in ME coefficient, irrespective of larger magnetization for higher Fe concentration, can be

understood based on the polarization results. As the polarization is a function of displacement of BO_6 octahedra in perovskite ferroelectrics, the continuous deviation from tetragonality for higher doping concentrations results in a deterioration of polar nature and hence ME coupling. Our results indicate that the crystal structure influences greatly to achieve larger ME outputs in single phase multiferroics. The present study illustrates that BCTZO with larger piezoelectric coefficient, due to the triple point, can be tuned to induce magnetism and ME cross coupling.

4. Conclusion

We have synthesized high purity Fe-doped BCTZO nanoparticles following a facile chemical synthesis method. XRD analysis confirms the MPB for undoped BCTZO composition and induced lattice strain for Fe-doped samples. A systematic decrease in tetragonality indicates a transformation from MPB phase to pseudo cubic. Raman spectroscopy further confirmed the compressive strain in the lattice and softening of tetragonal features (suppression of Raman mode around 295 cm^{-1}). The TEM/EDS studies further substantiated the presence of perovskite structure with expected elements in the final compound. Well saturated ferroelectric loops with systematic drop in polarization as well as increased coercivity, were observed for doped samples. Dielectric measurements showed a shift of T_C towards room temperature and disappearance of R-T transition for higher Fe doping. All these features were related to the systematic drop in grain size. By means of local piezoresponse measurements we observed the local imprint characteristics at nanoscale. The doped samples exhibited room temperature ferromagnetic properties and a maximum ME coefficient of 12.8

mV/cm-Oe for Fe-1 sample. The magnetic nature is analyzed based on the results of Mossbauer and XPS results and we conclude that the observed ferromagnetism is induced by oxygen vacancies arising from the iron doping.

Acknowledgements

The authors would like to acknowledge the financial support from FCT, Portugal (SFRH/BPD/75582/2010) and PEst-C/CTM/LA0025/2013 of FCT. This work was developed in the scope of the project CICECO-Aveiro Institute of Materials (Ref. FCT UID /CTM /50011/2013), financed by national funds through the FCT/MEC and when applicable co-financed by FEDER under the PT2020 Partnership Agreement and Post-doc grant of one of the authors (FF, SFRH/BPD/80663/2011).

1. Y. Tokura and S. Seki, *Adv. Mater.*, 2010, **22**, 1554.
2. M. Liu and N. X. Sun, *Phil. Trans. R. Soc. A*, 2014, **372**, 20120439.
3. K. Yue, R. Guduru, J. Hong, P. Liang, M. Nair and S. Khizroev, *PLoS ONE*, 2012, **7**, e44040.
4. C.-S. Park, A. Khachaturyan and S. Priya, *Appl. Phys. Lett.*, 2012, **100**, 192904.
5. H. A. Lu, L. A. Wills, B. W. Wessels, W. P. Lin, T. G. Zhang, G. K. Wong, D. A. Neumayer and T. J. Marks, *Appl. Phys. Lett.*, 1993, **62**, 1314.
6. S. G. Bahoosh, S. Trimper and J. M. Wesselinowa, *Phys. Status Solidi RRL*, 2011, **5**, 382.
7. A. Sundaresan and C. N. R. Rao, *Nano Today*, 2009, **4**, 96.
8. X. K. Wei, Y. T. Su, Y. Sui, Q. H. Zhang, Y. Yao, C. Q. Jin and R. C. Yu, *J. Appl. Phys.*, 2011, **110**, 114112.
9. N. V. Dang, T. D. Thanh, L. V. Hong, V. D. Lam and T.-L. Phan, *J. Appl. Phys.*, 2011, **110**, 043914.
10. S. Ray, P. Mahadevan, S. Mandal, S. R. Krishnakumar, C. S. Kuroda, T. Sasaki, T. Taniyama and M. Itoh, *Phys. Rev. B*, 2008, **77**, 104416.
11. X. K. Wei, T. Zou, F. Wang, Q. H. Zhang, Y. Sun, L. Gu, A. Hirata, M. W. Chen, Y. Yao, C. Q. Jin and R. C. Yu, *J. Appl. Phys.*, 2012, **111**, 073904.
12. F. Huang, Z. Jiang, X. Lu, R. Ti, H. Wu, Y. Kan and J. Zhu, *Appl. Phys. Lett.*, 2014, **105**, 022904.
13. L. Ju, T. Sabergharesou, K. G. Stamplecoskie, M. Hegde, T. Wang, N. A. Combe, H. Wu and P. V. Radovanovic, *J. Amer. Chem. Soc.*, 2012, **134**, 1136.
14. E. Venkata Ramana, S. M. Yang, R. Jung, M. H. Jung, B. W. Lee and C. U. Jung, *J. Appl. Phys.*, 2013, **113**, 187219.
15. W. Liu and X. Ren, *Phys. Rev. Lett.*, 2009, **103**, 257602.
16. D. Xue, Y. Zhou, H. Bao, C. Zhou, J. Gao and X. Ren, *J. Appl. Phys.*, 2011, **109**, 054110.
17. J. Gao, D. Xue, Y. Wang, D. Wang, L. Zhang, H. Wu, S. Guo, H. Bao, C. Zhou, W. Liu, S. Hou, G. Xiao and X. Ren, *Appl. Phys. Lett.*, 2011, **99**, 092901.
18. M. Yuan, L. Cheng, Q. Xu, W. Wu, S. Bai, L. Gu, Z. Wang, J. Lu, H. Li, Y. Qin, T. Jing and Z. L. Wang, *Adv. Mater.*, 2014, **26**, 7432.
19. R. B. V. D. A.C. Larson, *General Structure Analysis System (GSAS)*, Los Alamos National Laboratory Report LAUR, 2004.
20. B. H. Toby, *J. Appl. Cryst.*, 2001, **34**, 210.
21. E. Venkata Ramana, F. Figueiras, M. P. F. Graca and M. A. Valente, *Dalton Trans.*, 2014, **43**, 9934.
22. E. Venkata Ramana, A. Mahajan, M. P. F. Graça, S. K. Mendiratta, J. M. Monteiro and M. A. Valente, *Mater. Res. Bull.*, 2013, **48**, 4395.
23. W. Bai, X. J. Meng, T. Lin, L. Tian, C. B. Jing, W. J. Liu, J. H. Ma, J. L. Sun and J. H. Chu, *J. Appl. Phys.*, 2009, **106**, 124908.
24. M. Malinowski, K. Lukaszewicz and S. Asbrink, *J. Appl. Cryst.*, 1986, **19**, 7.

25. V. Polinger, P. Garcia-Fernandez and I. B. Bersuker, *Phys. B*, 2015, **457**, 296.
26. D. M. Tobaldi, R. C. Pullar, A. F. Gualtieri, M. P. Seabra and J. A. Labrincha, *Acta Materialia*, 2013, **61**, 5571.
27. U. D. Venkateswaran, V. M. Naik and R. Naik, *Phys. Rev. B*, 1998, **58**, 14256.
28. D. Damjanovic, A. Biancoli, L. Batooli, A. Vahabzadeh and J. Trodahl, *Appl. Phys. Lett.*, 2012, **100**, 192907.
29. J. Pokorny, U. M. Pasha, L. Ben, O. P. Thakur, D. C. Sinclair and I. M. Reaney, *J. Appl. Phys.*, 2011, **109**, 114110.
30. J. W. Bennett, I. Grinberg, P. K. Davies and A. M. Rappe, *Phys. Rev. B*, 2010, **82**, 184106.
31. G. Arlt, *Ferroelectrics*, 1990, **104**, 217.
32. C. A. Randall, N. Kim, J.-P. Kucera, W. Cao and T. R. Shrout, *J. Amer. Ceram. Soc.*, 1998, **81**, 677.
33. C. E. Ciomaga, M. T. Buscaglia, M. Viviani, V. Buscaglia, L. Mitoseriu, A. Stancu and P. Nanni, *Phase Transitions*, 2006, **79**, 389.
34. Z. Zhao, V. Buscaglia, M. Viviani, M. T. Buscaglia, L. Mitoseriu, A. Testino, M. Nygren, M. Johnsson and P. Nanni, *Phys. Rev. B*, 2004, **70**, 024107.
35. Y. Wu and G. Cao, *J. Mater. Res.*, 2000, **15**, 1583.
36. G. Arlt, D. Hennings and G. de With, *J. Appl. Phys.*, 1985, **58**, 1619.
37. S. Batakrushna, P. K. Giri, I. Kenji and F. Minoru, *J. Phys. D: Appl. Phys.*, 2014, **47**, 215302.
38. H. Chermette, P. Pertosa and F. M. Michel-Calendini, *Chem. Phys. Lett.*, 1980, **69**, 240.
39. Y. Shuai, S. Zhou, D. Bürger, H. Reuther, I. Skorupa, V. John, M. Helm and H. Schmidt, *J. Appl. Phys.*, 2011, **109**, 084105.
40. N. Balke, P. Maksymovych, S. Jesse, A. Herklotz, A. Tselev, C.-B. Eom, I. I. Kravchenko, P. Yu and S. V. Kalinin, *ACS Nano*, 2015, **9**, 6484.
41. J. M. D. Coey, A. P. Douvalis, C. B. Fitzgerald and M. Venkatesan, *Appl. Phys.Lett.*, 2004, **84**, 1332.
42. Z. Ren, G. Xu, X. Wei, Y. Liu, X. Hou, P. Du, W. Weng, G. Shen and G. Han, *Appl. Phys. Lett.*, 2007, **91**, 063106.
43. J. Shah and R. K. Kotnala, *J. Mater. Chem. A*, 2013, **1**, 8601.
44. J. J. Beltrán, J. A. Osorio, C. A. Barrero, C. B. Hanna and A. Punnoose, *J. Appl. Phys.*, 2013, **113**, 17C308.
45. F. Lin, D. Jiang, X. Ma and W. Shi, *Physica B: Condensed Matter*, 2008, **403**, 2525.
46. D. Cao, M. Q. Cai, Y. Zheng and W. Y. Hu, *Phys. Chem. Chem. Phys.*, 2009, **11**, 10934.
47. T. Shimada, J. Wang, T. Ueda, Y. Uratani, K. Arisue, M. Mrovec, C. Elsässer and T. Kitamura, *Nano Lett.*, 2015, **15**, 27.
48. K. C. Verma, V. Gupta, J. Kaur and R. K. Kotnala, *J. Alloys Compd.*, 2013, **578**, 5-11.
49. M. Kumari, C. Prakash and R. Chatterjee, *J. Appl. Phys.*, 2013, **113**, 17D918.

Fig. 1 (a) XRD θ-2θ scan of Fe-0, Fe-1, Fe-2 and Fe-5 sintered at 1400 ^{o}C. Inset: composition dependence of (101)/(110) and (002)/(200) peak splittings.

Fig. 2 Rietveld graphical output of (a) Fe-0 and (b) Fe-5 samples. The black open squares represent the observed pattern, the continuous red line represents the calculated pattern, and the difference curve between the observed and calculated profiles is given by the blue continuous line plotted below. The positions of reflections are indicated by the small vertical bars (black: T phase; red: R phase). Inset: 3D rendering in the ball-and-stick and polyhedron models, using the structural data obtained from GSAS, of the T phase. The small dark grey spheres represent O, the bigger light-blue sphere Ti (fractions of Zr and Fe are shown in dark green, and brown colours, respectively), whilst the bigger green sphere is Ba (fraction of Ca in turquoise colour).

Fig. 3 HRTEM image of Fe-2 nanoparticles. Inset: fringe width of 0.282 nm corresponds to the d spacing of {110} reflection of tetragonal BTO lattice. (b) TEM-EDS of Fe-2 nanoparticles. The presence of Ba, Ca, Ti, Zr, Fe elements can be seen. Here, Cu peak is from the grid used for measurements.

Fig. 4 (a) Room temperature Raman spectra of different Fe doped BCTZO samples in the range 100-1000 cm^{-1}. (b) Variation of A_{1g} mode with composition.

Fig. 5 UV-Vis diffuse reflectivity spectra of Fe-doped BCTZO. Inset: band gap energy calculation from absorption vs. photon energy. Black line indicates the X-axis intercept.

Fig. 6 Scanning electron microscopy images of BCTZO samples with different Fe concentrations. Here a, b, c and d corresponds to undoped, 1 mol. %, 2 mol. % and 5 mol. % Fe doped BCTZO.

Fig. 7 (a) Permittivity as a function of temperature measured at 1 kHz for (1) Fe-0, (2) Fe-1, (3) Fe-2 and (4) Fe-5 samples. Inset: dielectric dispersion with temperature. Arrow indicates the frequency increase. (b) log $(1/\varepsilon_r' - 1/\varepsilon_r'_{max})$ vs. log $(T-T_m)$ plot at 1 kHz.

Fig. 8 (a) Room temperature P-E loops for different Fe doped BCTZO samples. Inset: electric field dependence of P_r. (b) Electric field dependence of polarization current (I_P) for Fe-0 and Fe-5 samples.

Fig. 9 Ti 2p core-level XPS spectra of Fe-0 and Fe-5 samples. Inset: O1s XPS spectra of Fe-0 and Fe-5 samples with Lorentzian fitting.

Fig.10 Local piezoresponse images of Fe-2 sample: (a) topography, (b, d) amplitude response before and after electrical poling, (c, e) phase response before and after electrical poling. Here red and black squares represent poled areas with positive and negative voltages of 20 V DC. (f) Local piezoresponse hysteresis loops for Fe-0, Fe-1, Fe-2 and Fe-5 samples.

Fig.11 (a) Magnetic hysteresis loops for Fe-0, Fe-1, Fe-2 and Fe-5. Inset: low-field hysteresis loops showing H_C. (b) Temperature dependence of magnetization for Fe-1 sample. Inset: M-H relation at different temperatures.

Fig.12 Room temperature Mossbauer spectra of Fe-2 and Fe-5 samples. Mossbauer parameters such as Isomer shifts (δ), quadrupole splittings (Δ) and line widths (Γ) were calculated from the fitting.

Fig. 13. Variation of ME coefficient with bias magnetic field superimposed by an ac magnetic field of 1 Oe (1 kHz).

Table 1 Rietveld agreement factors and phase composition of pure and doped BCTZO [a]

Sample	No. of variables	Agreement factors			Phase composition (wt.%)	
		$R(_F^2)$ (%)	R_{wp} (%)	χ^2	Tetragonal (*P*4*mm*)	Rhombohedral (*R*3*m*)
Fe-0	18	8.17	8.31	5.98	61.4(2)	38.6(3)
Fe-1	19	8.48	10.66	5.53	90.8(1)	9.2(5)
Fe-2	18	6.01	7.57	4.08	92.3(1)	7.7(2)
Fe5	14	8.34	9.25	4.51	100	–

[a] There were 7918 observations for every refinement; the number of tetragonal and rhombohedral reflections was 84 and 88, respectively. Values in parentheses are the standard deviations, referred to the last decimal figure.

Table 2 Unit cell and structural parameters of the tetragonal (space group *P*4*mm*) and rhombohedral (space group *R*3*m*) phases, as obtained from the Rietveld crystal structural refinements.

Sample	**Symmetry** **Unitcell parameters**	**Site** **(Wyckoff position)**	**Position** ***x***	 ***y***	 ***z***	U_{iso} **(Å^2)**[a]
Fe-0	**Tetragonal**	Ba(1*a*)	0	0	0	1.17(4)
	$a = b = 3.9715(1)$ Å	Ti(1*b*)	½	½	0.515(3)	1.00(8)
	$c = 4.0070(1)$ Å	O1(1*b*)	½	½	−0.065(4)	0.60(3)
	$c/a = 1.0089$	O2(2*c*)	½	0	0.445(3)	0.64(2)
	Volume = 63.20(1) Å^3					
	Rhombohedral	Ba(3*a*)	0	0	0	0.82(11)
	$a = 4.0121(4)$ Å	Ti(18*c*)	0.498(5)	0.498(5)	0.498(5)	0.37(17)
	$\alpha = \beta = \gamma = 89.58(1)°$	O(18*c*)	0.543(3)	0.543(3)	0.013(3)	0.15(3)
Fe-1	**Tetragonal**	Ba(1*a*)	0	0	0	0.33(4)
	$a = b = 4.0016(1)$ Å	Ti(1*b*)	½	½	0.483(2)	0.50(7)
	$c = 4.0231(1)$ Å	O1(1*b*)	½	½	−0.025(6)	0.74(5)
	$c/a = 1.0054$	O2(2*c*)	½	0	0.508(8)	0.91(2)
	Volume = 64.43(1) Å^3					
	Rhombohedral	Ba(3*a*)	0	0	0	0.01(5)
	$a = 4.0084(1)$ Å	Ti(18*c*)	0.478(4)	0.478(4)	0.478(4)	0.74(4)
	$\alpha = \beta = \gamma = 90.05(1)°$	O(18*c*)	0.551(8)	0.551(8)	0.058(11)	0.48(4)
Fe-2	**Tetragonal**	Ba(1*a*)	0	0	0	0.36(1)
	$a = b = 4.0020(1)$ Å	Ti(1*b*)	½	½	0.477(1)	0.26(5)
	$c = 4.0203(1)$ Å	O1(1*b*)	½	½	−0.033(4)	0.55(5)
	$c/a = 1.0046$	O2(2*c*)	½	0	0.535(2)	0.44(3)
	Volume = 64.39(1) Å^3					
	Rhombohedral	Ba(3*a*)	0	0	0	3.37(27)
	$a = 4.0074(1)$ Å	Ti(18*c*)	0.490(7)	0.490(7)	0.490(7)	1.89(40)
	$\alpha = \beta = \gamma = 89.95(1)°$	O(18*c*)	0.673(7)	0.673(7)	0.271(11)	0.54(15)
Fe-5	**Tetragonal**	Ba(1*a*)	0	0	0	0.15(2)
	$a = b = 4.0131(1)$ Å	Ti(1*b*)	½	½	0.500(7)	0.44(4)
	$c = 4.0041(1)$ Å	O1(1*b*)	½	½	−0.006(22)	2.24(29)
	$c/a = 0.9978$	O2(2*c*)	½	0	0.467(5)	0.02(20)
	Volume = 64.49(1) Å^3					

[a] Given as $100 \times U_{iso}$.

Table 3 A−O, B−O length distances, and average $\langle B-O\rangle$ length distance; in columns 4 and 5 are described the distortion index (D) of octahedron, the quadratic elongation (QE) of BO_6 in the tetragonal phase.

Sample	Bond length (Å)	*D*	QE
Fe-0 [a]		0.054	1.022
A−O1 (4×)	2.82043(6)		
A−O2 (4×)	2.98229(6)		
A−O2 (4×)	2.66798(5)		
B−O1	2.32737(7)		
B−O1	1.67957(5)		
B−O2 (4×)	2.00585(4)		
$\langle B-O\rangle$	2.0050(1)		
Fe-1 [a]		0.006	1.002
A−O1 (4×)	2.83132(2)		
A−O2 (4×)	2.81473(1)		
A−O2 (4×)	2.85975(1)		
B−O1	2.04290(1)		
B−O1	1.98017(1)		
B−O2 (4×)	2.00332(1)		
$\langle B-O\rangle$	2.0061(1)		
Fe-2 [a]		0.007	1.009
A−O1 (4×)	2.8329(7)		
A−O2 (4×)	2.739(6)		
A−O2 (4×)	2.937(6)		
B−O1	2.050(16)		
B−O1	1.971(16)		
B−O2 (4×)	2.0146(11)		
$\langle B-O\rangle$	2.0131(14)		
Fe-5 [a]		0.005	1.003
A−O1 (4×)	2.83777(2)		
A−O2 (4×)	2.92935(3)		
A−O2 (4×)	2.74275(2)		
B−O1	2.02743(3)		
B−O1	1.97670(3)		
B−O2 (4×)	2.01092(2)		
$\langle B-O\rangle$	2.0080(1)		

[a] A = Ba, Ca in all the samples; B = Ti, Zr in BCTZO, and Ti, Zr, Fe in Fe-1, Fe-2, and Fe-5.

Table 4 Mossbauer parameters of Fe-2 and Fe-5 samples: δ is isomer shift, Δ is quadrupole splitting, Γ is the Lorentzian line width and area is relative area.

	δ (mm/s)	**Δ (mm/s)**	**Γ (mm/s)**	**Area %**
Fe-2 sample				
Site I (Fe3+)	0.39(1)	0.52(1)	0.50(1)	66.0
Site II (Fe3+)	0.37(1)	1.22(1)	0.70(1)	29.8
Site III (Fe3+)	0.42(1)	-	0.50(1)	5.2
Fe-5 sample				
Site I (Fe3+)	0.38(1)	0.54(1)	0.52(1)	80.7
Site II (Fe3+)	0.32(1)	1.27(1)	0.71(1)	19.2

Fig. 1

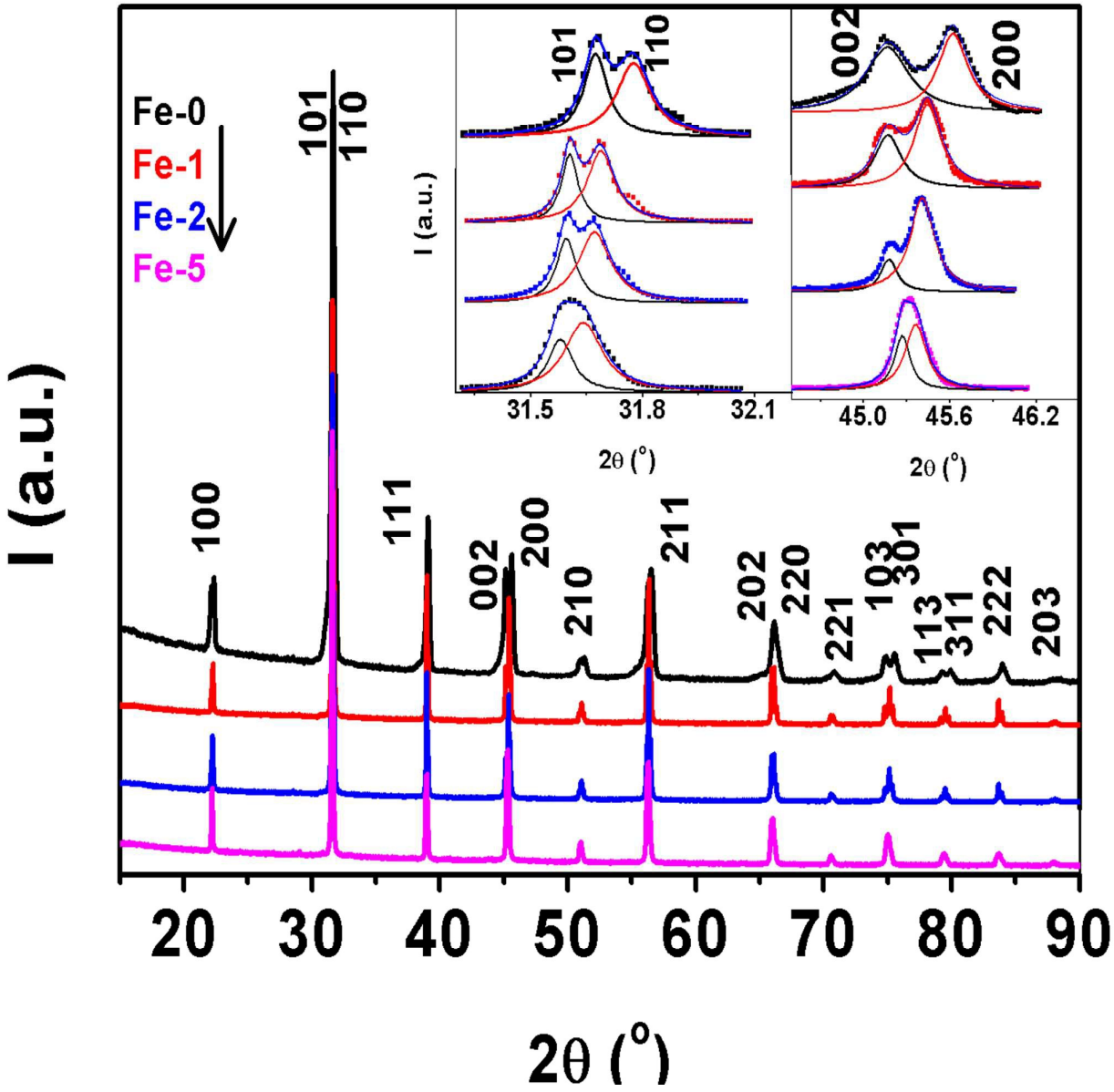

Fig. 2

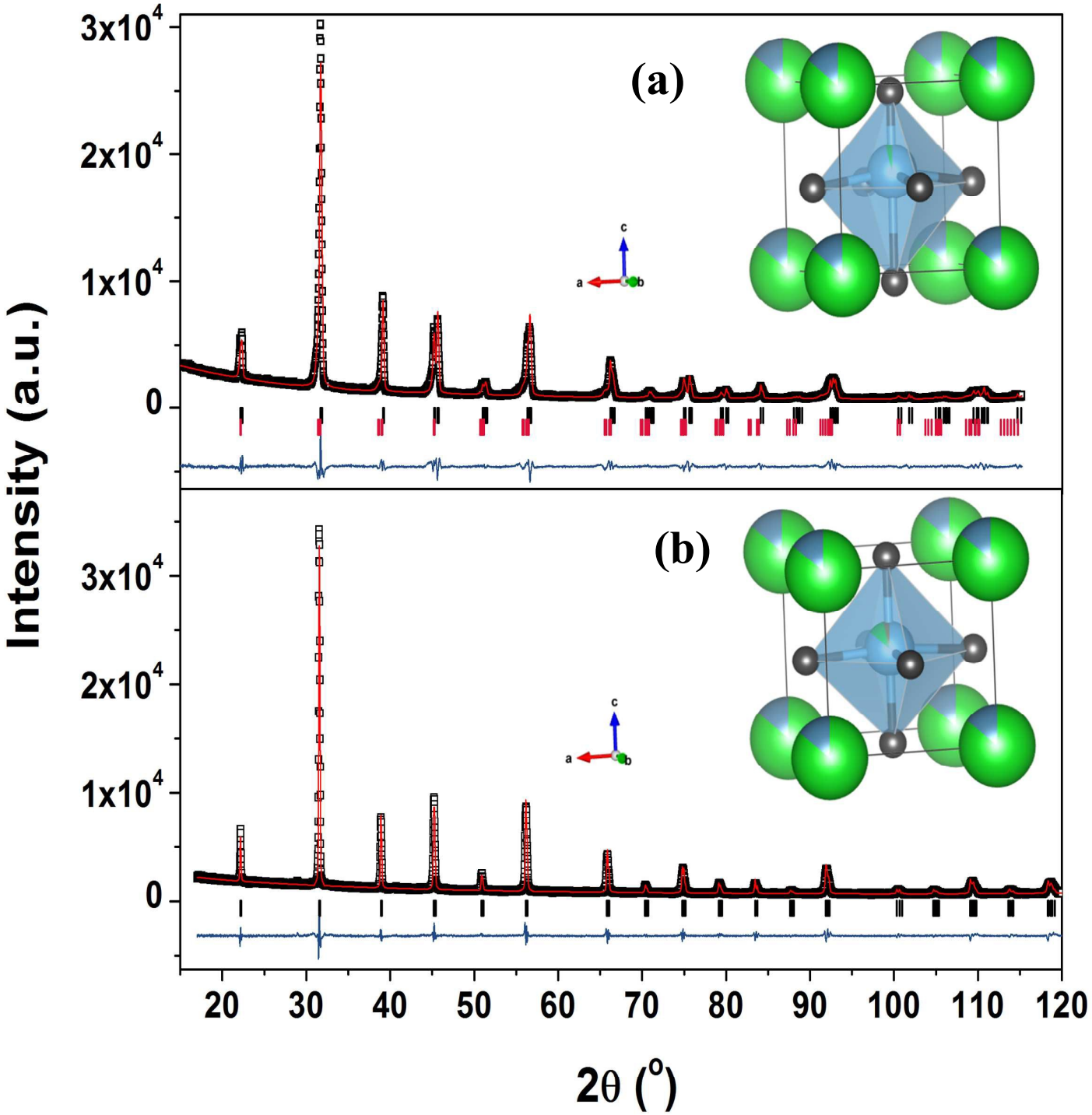

Fig. 3

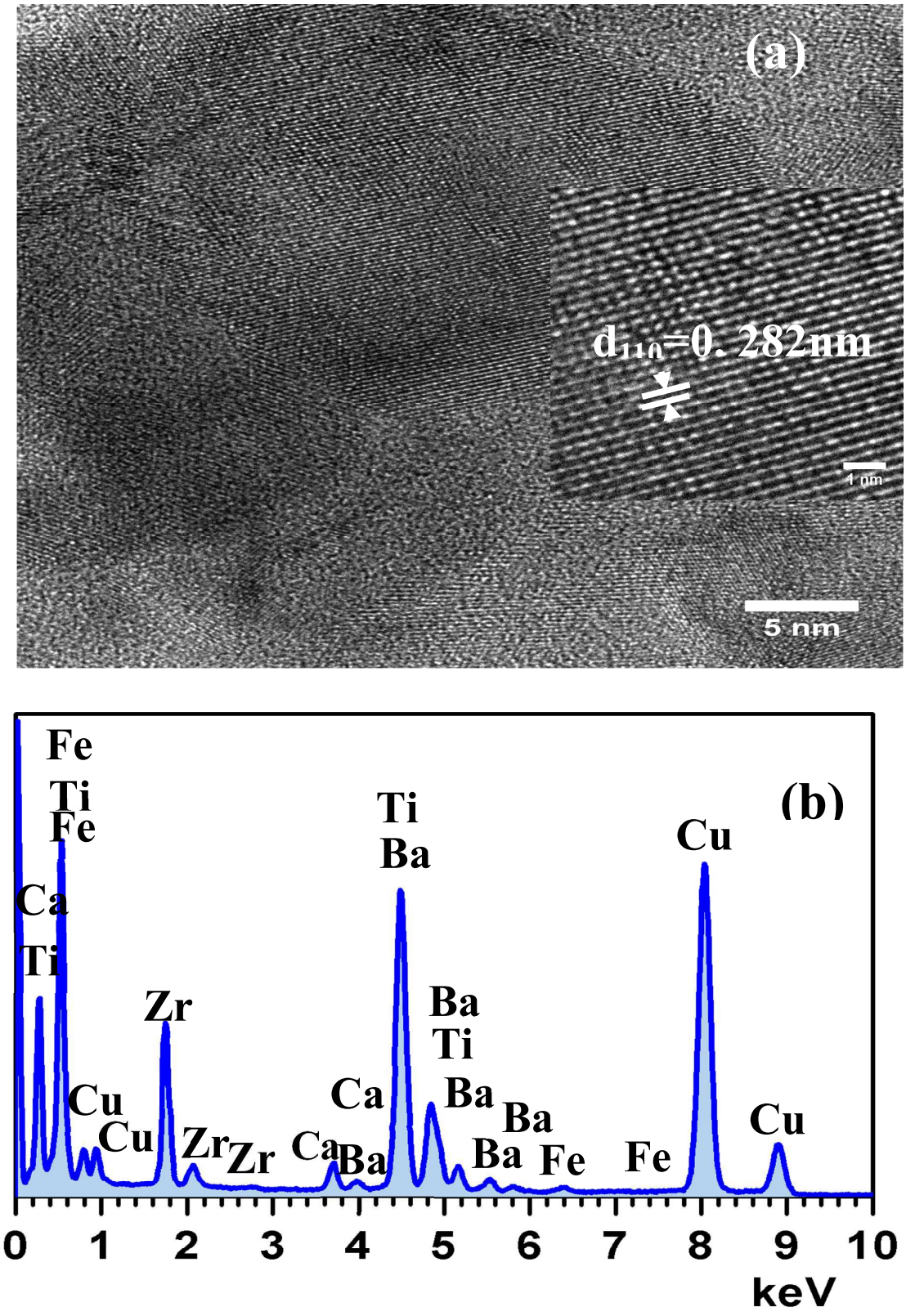

Fig. 4

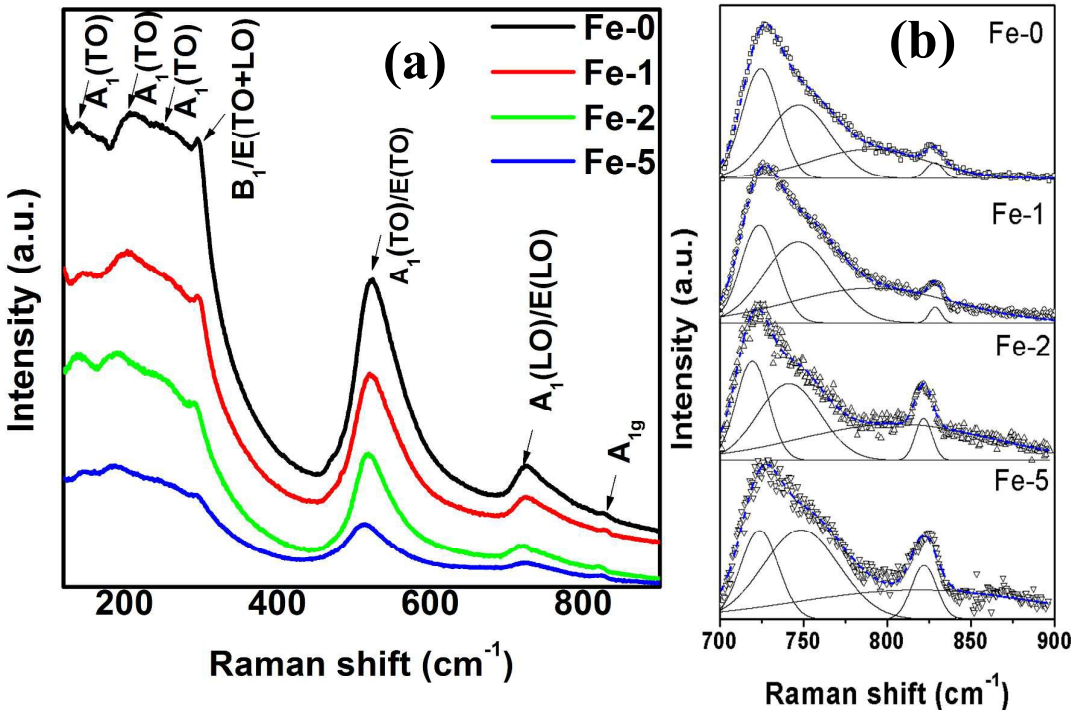

Fig. 5

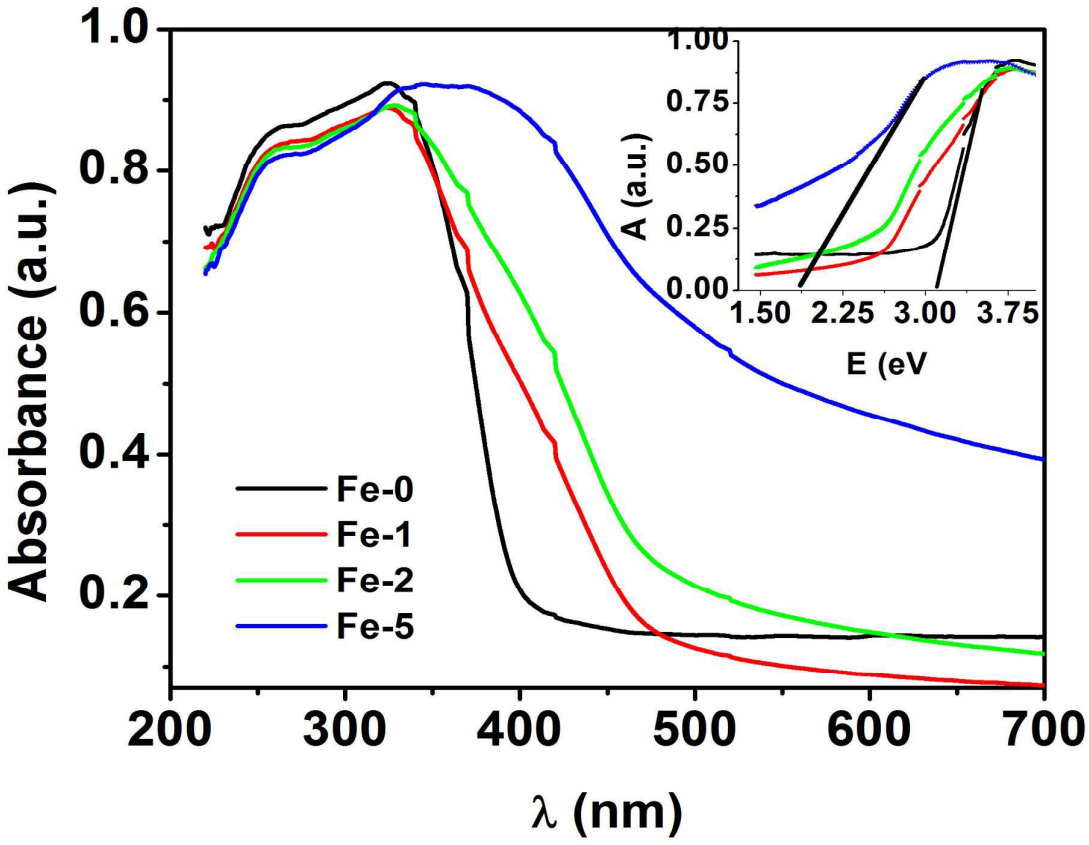

Fig. 6

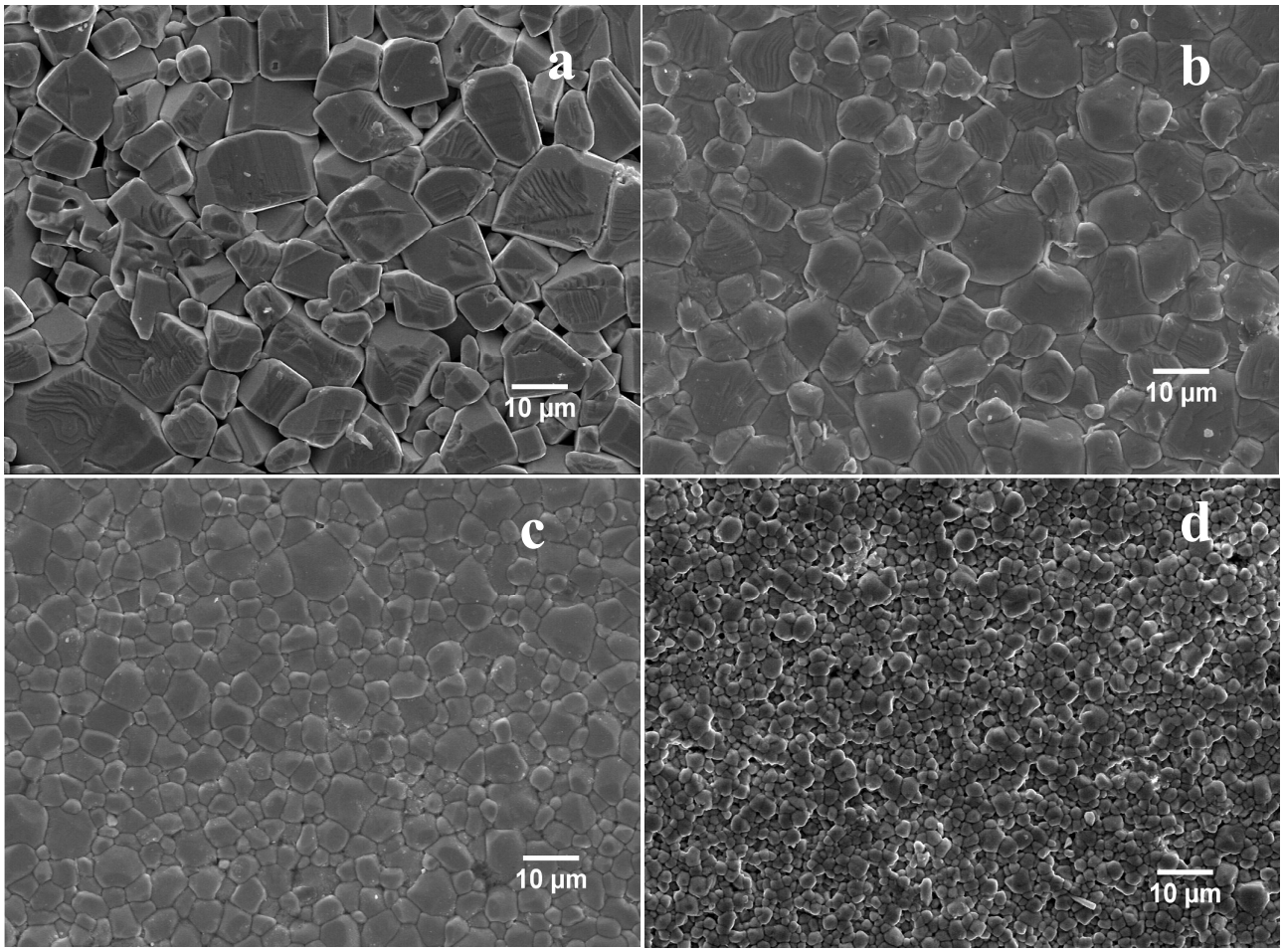

Fig. 7

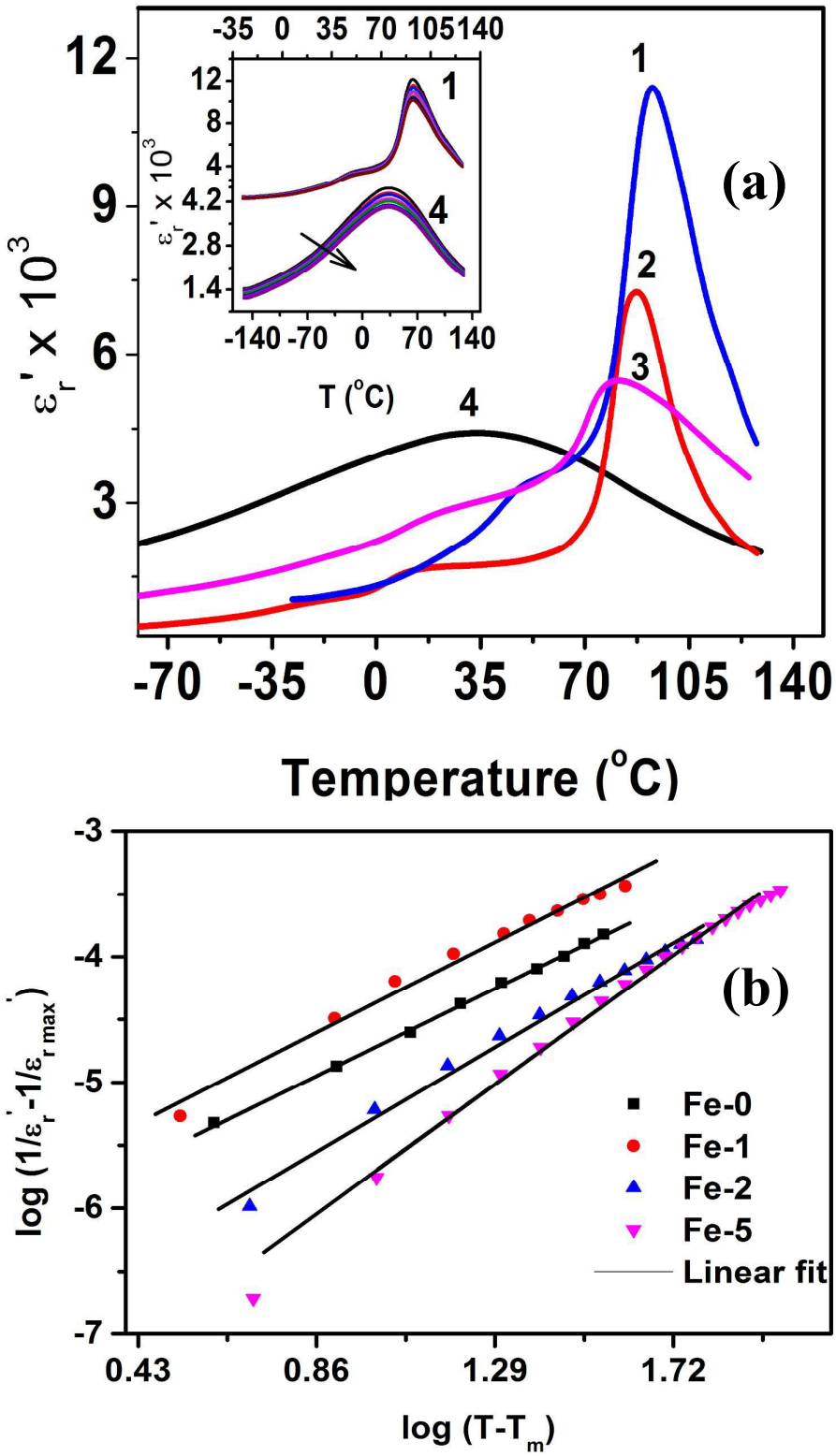

Fig. 8

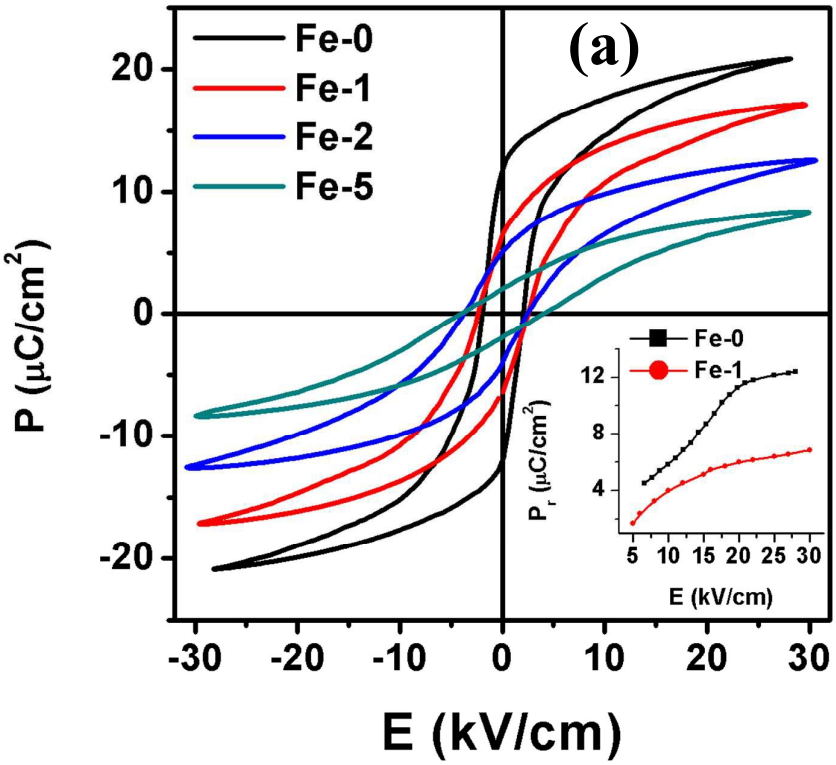

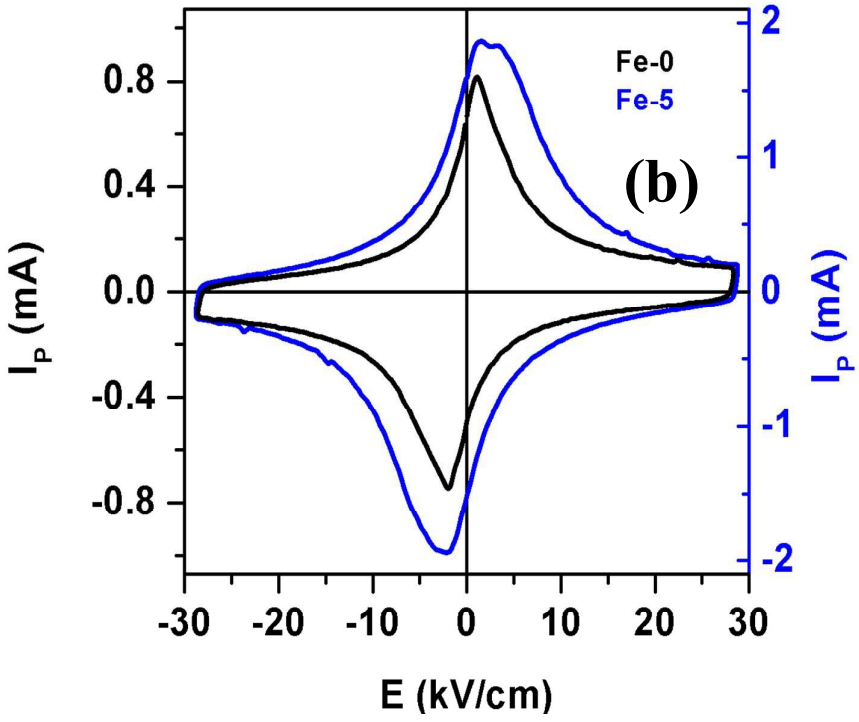

Fig. 9

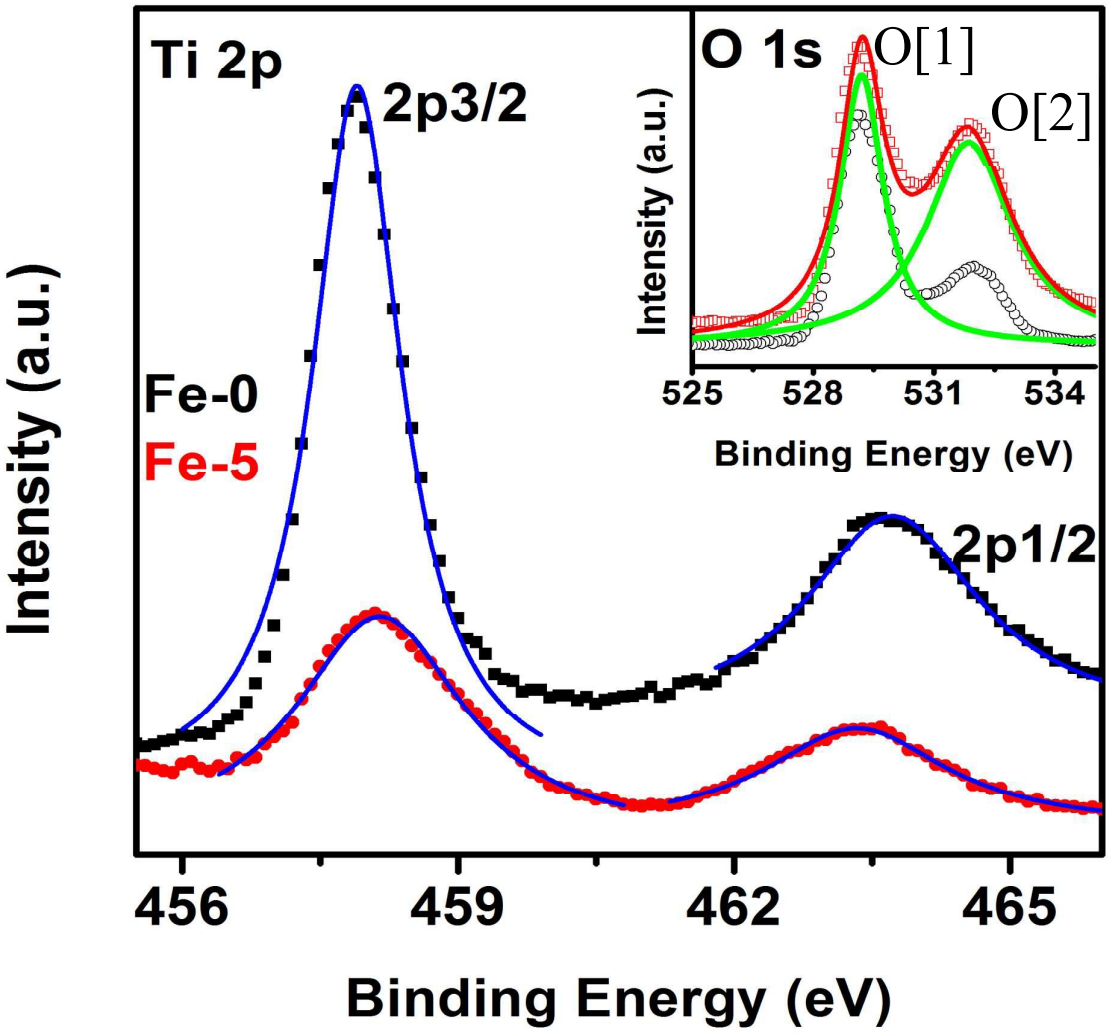

Fig. 10

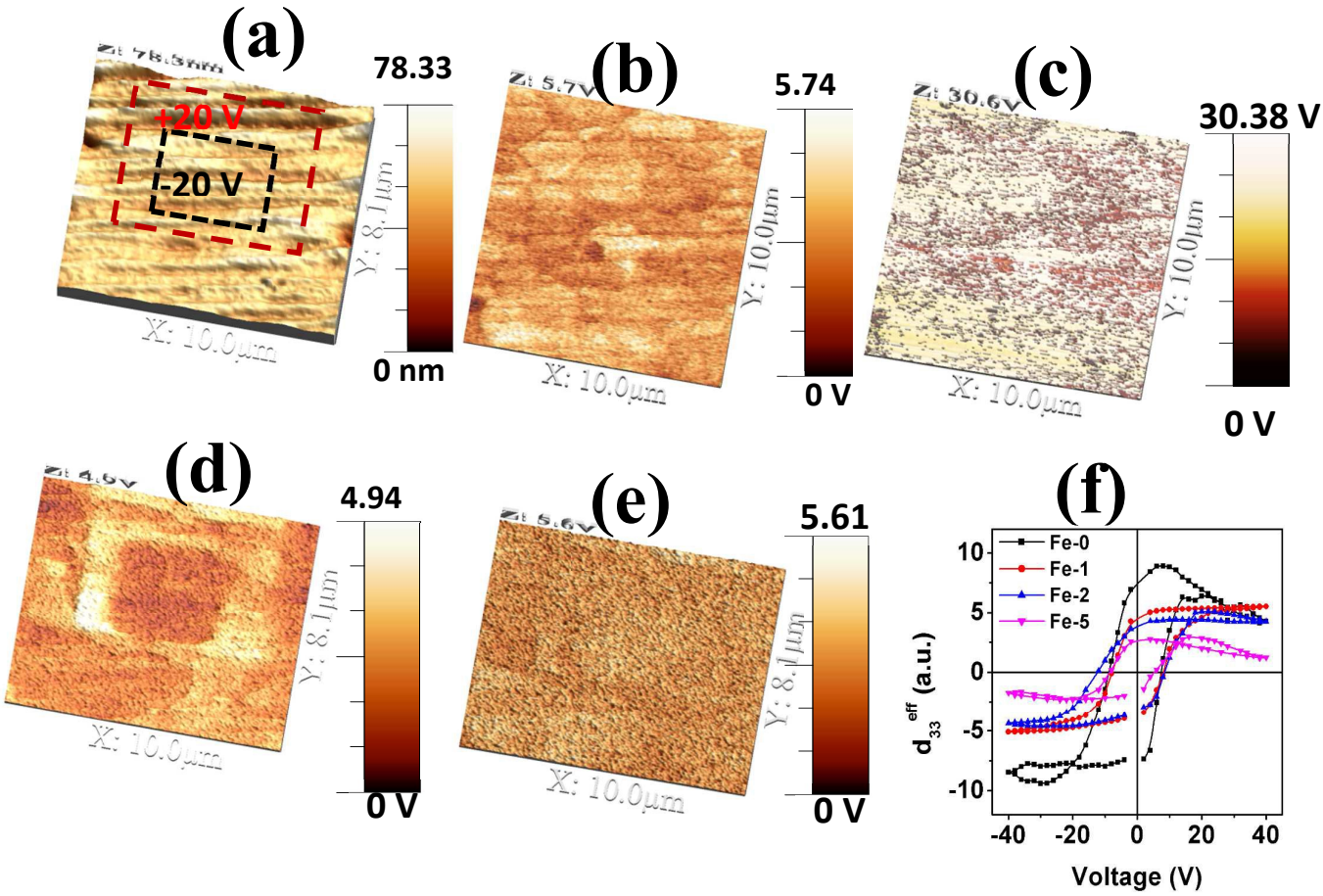

Fig. 11

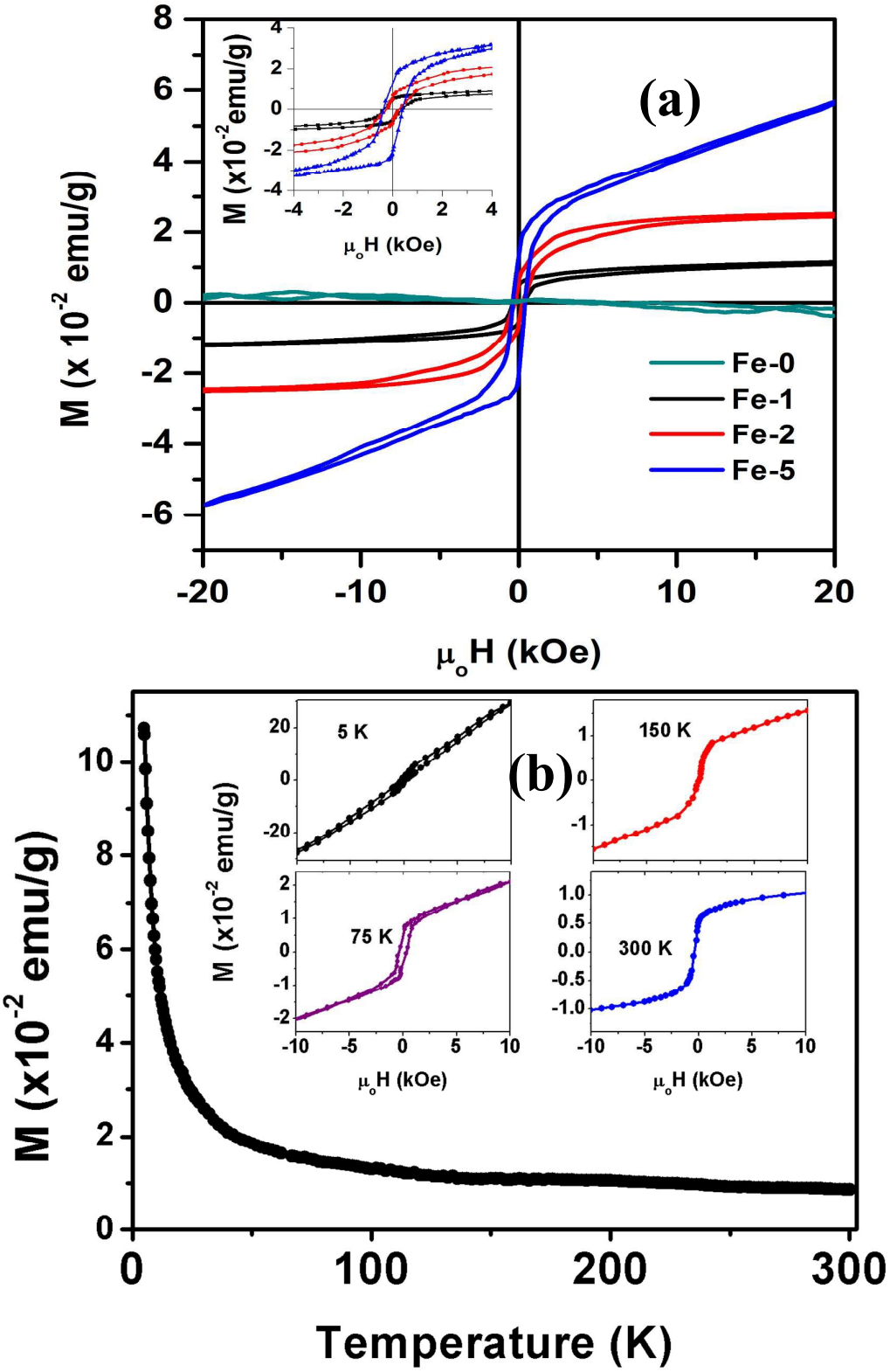

Fig. 12

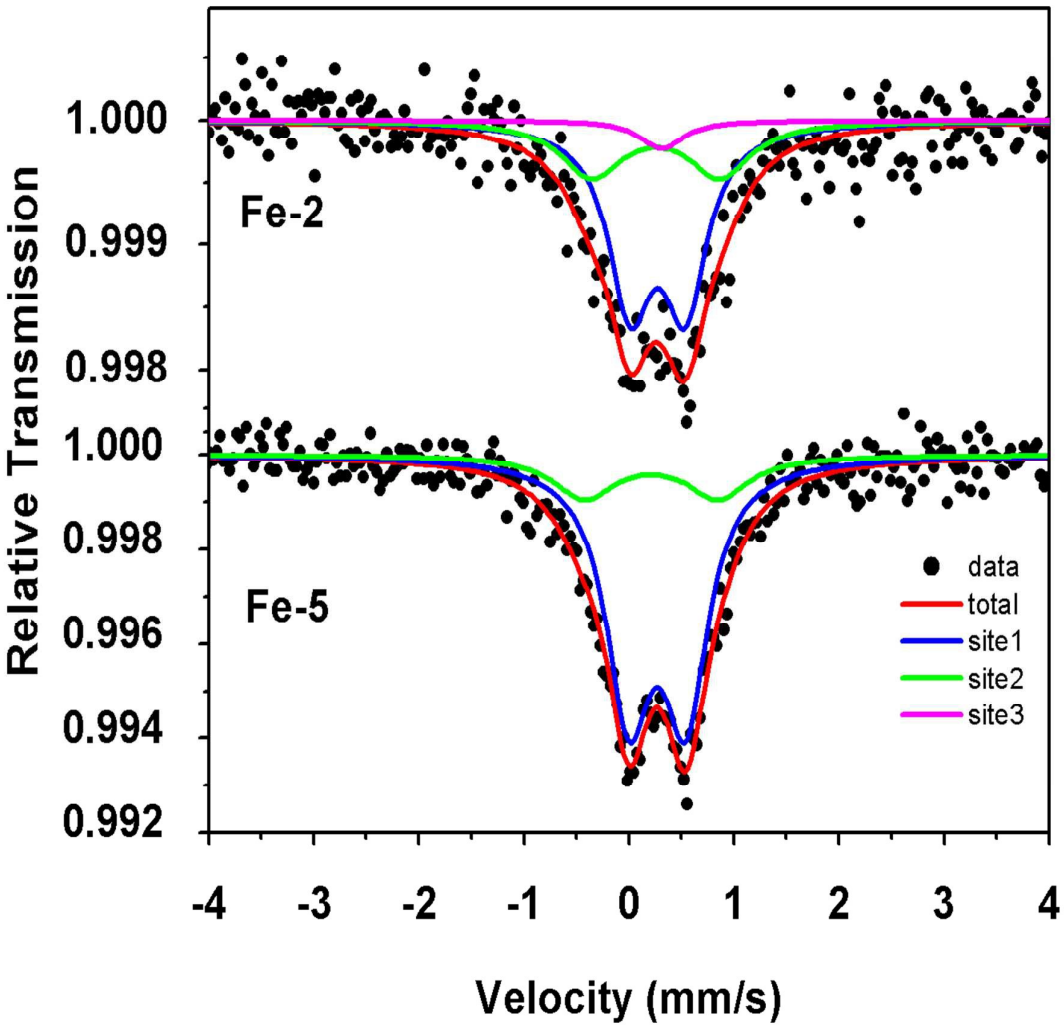

Fig. 13